Effects of ion irradiation on Mercury terrestrial analogues in the visible to mid-infrared

Emma Caminiti, Cateline Lantz, S Besse, Rosario Brunetto, C Carli, L Serrano, N Mari, Mathieu Vincendon, Alain Doressoundiram

Effects of ion irradiation on Mercury terrestrial analogues in the visible to mid-infrared

E.Caminiti[1], C.Lantz[2], S.Besse[3], R.Brunetto[2], C.Carli[4], L.Serrano[5], N.Mari[6], M.Vincendon[2], A.Doressoundiram[1]

Corresponding author: E.Caminiti (emma.caminiti@obspm.fr)

[1]LESIA, Observatoire de Paris, Université PSL, CNRS, Sorbonne Université, Université de paris, 5 place Jules Janssen, 92195 Meudon, France.
[2]Institut d'Astrophysique Spatiale, Université Paris- Saclay, CNRS, 91400 Orsay, France.
[3]European Space Agency (ESA), European Space Astronomy Centre (ESAC), Camino Bajo del Castillo s/n, Villanueva de la Cañada, 28692 Madrid, Spain
[4]IAPS-INAF, Via Fosso del Cavaliere, 100, 00133 Rome, Italy.
[5]Independent researcher. 660001 Pereira, Colombia.
[6]Department of Earth and Environmental Sciences, University of Pavia, 27100 Pavia, Italy.

Keywords: Mercury, Spectroscopy, Experimental techniques, Surface processes, Solar wind

Highlights:

- Ion irradiation is at the origin of an exponential darkening, a reddening and a flattening of VNIR spectra of Mercury volcanic terrestrial analogues.
- MIR features like the Christiansen feature and Reststrahlen bands are shifted due to ion irradiation.
- The alteration of spectroscopic features is closely influenced by the composition and will likely participate in the origin of spectral heterogeneities on Mercury.
- After a certain irradiation dose/time exposure spectral differences among units on Mercury may be limited by the saturation of the surface.

The surface of Mercury is subject to space weathering that complicates remote sensing data analysis. We present an experimental study performed on Mercury volcanic surface analogues to provide a better constraint on spectral alterations induced by solar wind. We used 20 keV He^+ with fluences up to 5 x 10^{17} ions/cm^2 to simulate ion irradiation reaching the surface. Terrestrial ultramafic lava already identified as good analogues for Mercury were used: a boninite, a basaltic komatiite and a komatiite. Spectra were acquired in the visible to mid-infrared (VMIR) wavelength range, between 0.4 and 16 µm. Spectral alterations induced by irradiation are observed. In the visible to near-infrared (VNIR) samples show an exponential darkening, a reddening and a flattening of spectra. Above a certain irradiation dose (1 x 10^{17} ions/cm^2 in our conditions), the darkening reaches a plateau while the reddening and flattening do not show any definable trend. In the mid-infrared (MIR) we observe a shift of Reststrahlen bands towards longer wavelengths (≤0.42 µm). The Christiansen feature is shifted towards longer or shorter wavelengths according to the irradiation dose (≤0.2 µm). The spectral alteration is closely influenced by the composition. As Mercury's surface is compositionally heterogeneous, the degree of spectral alteration varies on the planet and putatively participates in the heterogeneous spectral properties of the surface. This work provides ground-truth data for future ESA-JAXA-

BepiColombo observations. The alteration of VMIR spectral features induced by ion irradiation simulated in the laboratory will be used for future SIMBIO-SYS (Spectrometer and Imaging for MPO BepiColombo Integrated Observatory SYStem) and MERTIS (Mercury Radiometer and Thermal Infrared Spectrometer) data analysis.

1. Introduction

Mercury's surface, as well as other atmosphere-free bodies, is subject to space weathering (SpWe). SpWe includes processes occurring in the space environment that alter the observable mineralogical, physical and chemical properties of a surface over time. Solar wind electrons and ions (Meyer-Vernet, 2007), solar photons, cosmic radiation and impacts are part of this phenomenon. Mercury's global environment and SpWe were described by Domingue et al. (2014) and compared with other airless bodies in Pieters and Noble (2016). Contrary to the Moon and asteroids, Mercury's internal magnetic field influences solar wind-surface interactions (Ogilvie et al., 1974; Lavorenti et al., 2023). However, this magnetic field being weak solar wind access to the surface may be only slightly lower than at the Moon (Domingue et al., 2014). Moreover, because of a faster SpWe than regolith overturn, we expect more SpWe-derived products on Mercury than on the Moon (McKay et al., 1991; Killen et al., 2007; Lucey and Riner, 2011).

SpWe, including ion irradiation, can introduce a bias in the analysis of remote sensing data (Nittler et al., 2004). In the visible to the near-infrared (VNIR) wavelength range, SpWe modifies spectral features by changing the spectral albedo (decreasing the reflectance: darkening or increasing the reflectance: brightening), the slope of the reflectance spectrum (increasing slope towards longer wavelengths: reddening, increasing slope towards shorter wavelengths: blueing) and by reducing spectral contrasts (Brunetto and Strazulla, 2005; Brunetto et al., 2006; Loeffler et al., 2009; Lantz et al., 2015, 2017; Pieters and Noble, 2016; Pentillä et al., 2020; Rubino et al., 2024). In the mid-infrared (MIR) wavelength range, bands are very sensitive to SpWe (Lantz et al., 2017; Brunetto et al., 2020). Irradiation induces an alteration in band profiles and a shift of the Christiansen Feature (CF) as well as the Reststrahlen Bands (RBs) and the Transparency Feature (TF) (Vernazza et al., 2013; Brunetto et al., 2014, 2020; Jäggi et al., 2021; Lantz et al., 2015,2017). Understanding spectral alterations induced by SpWe is necessary to analyse remote sensing data and decouple the intrinsic properties of the surface from the effect of the space environment.

On Mercury, specific spectral features like hollows (Barraud et al., 2020, 2023) and spectral differences between color units (Caminiti et al., 2023) can be explained by the difference in compositions. Nevertheless, on a global scale spectral colour units (Robinson et al., 2008; Denevi et al., 2009; Ernst et al., 2010; D'Incecco et al., 2015; Murchie et al., 2015) and compositional units (Weider et al., 2012, 2014, 2015; Peplowski et al., 2015; Peplowski and Stockstill-Cahill, 2019; Namur & Charlier, 2017; Vander Kaaden et al., 2017; Wilson et al., 2019; Nittler et al., 2020) are not necessarily correlated highlighting that the composition is not the only parameter at the origin of spectral heterogeneities (Weider et al., 2014; Riner and Lucey, 2012). SpWe is not expected to produce the same effects on surfaces of different compositions and has to be considered while studying the diversity of spectral and compositional units and their origins (Fu et al., 2012; Riner and Lucey, 2012; Chrbolková et al., 2021). The elemental composition of the surface will directly be affected by SpWe as solar wind interaction processes lead to material removal such as light elements (Nittler et al., 2001). Constraining the effect of SpWe is necessary to reconstruct the geological history of the planet using compositional and spectral data.

Laboratory studies have been done to characterise good analogues representing the diversity of geochemical units on Mercury (Carli et al., 2013; Morlok et al., 2017, 2019, 2021, 2023; Weber et al., 2019; Reitze et al., 2021; Mari et al., 2023). Additional works have shown the importance of the physical properties of the surface in the understanding of spectral properties (Jäggi et al., 2021; Bruschini et al., 2022; Pisello et al., 2023). The effects of extreme temperatures on Mercury have also been investigated on varied analogues (Benthley, 2005; Helebert et al., 2013; Maturilli et al., 2014; Bott et al., 2023a). However, even if some studies analysed the effect of micrometeorite bombardment (Benthley, 2005; Sasaki and Kurahashi, 2004; Weber et al., 2019; Thompson et al., 2021; Bott et al., 2023b) less has been done concerning spectral alterations induced by the solar wind under Mercury's conditions (Jäggi et al., 2021). Jäggi et al. (2021) have noted significant spectral alterations induced by ion irradiation in the MIR highlighting the necessity to deeper investigate SpWe under Mercury's conditions using a higher energy.

Ion irradiation on airless bodies has already been simulated in the laboratory especially concerning asteroids and minerals (Brunetto and Strazzulla, 2005; Loeffler et al., 2009; Fu et al., 2012; Vernazza et al., 2013; Brunetto et al., 2014, 2020; Lantz et al., 2015; 2017; Chrbolková et al., 2021; Jäggi et al., 2021; Rubino et al., 2024). Results from Mariner

10 (Dunne and Burgess, 1978) and the MErcury Surface, Space ENvironment, GEochemistry, and Ranging (MESSENGER) (McNutt et al., 2006; Solomon et al., 2007) missions have shown that the surface of Mercury has been molded by volcanism (Denevi et al., 2013; Byrne et al., 2016; Wright et al., 2021). From a morphological point of view, notably through the study of Borealis Planitia, komatiite has quickly been proposed as a good lava analogue (Head et al., 2011). The surface elemental composition of Mercury revealed by MESSENGER is heterogeneous leading to the definition of several geochemical terranes (Weider et al., 2012, 2014, 2015; Peplowski et al., 2015; Peplowski and Stockstill-Cahill, 2019; Wilson et al., 2019; Vander Kaaden et al., 2017; Nittler et al., 2020). In the absence of direct measurements of mineralogical composition, geochemical models have estimated the mineralogy of the surface. They concluded that Mercury's surface can be compared to terrestrial boninite and komatiite (Nittler et al., 2011; Stockstill-Cahill et al., 2012; Weider et al., 2012, 2015; Charlier et al., 2013; Vander Kaaden and McCubbin, 2016; Vander Kaaden et al., 2017; Peplowski and Stockstill-Cahill, 2019). In the absence of Mercury's samples, these terrestrial lavas represent good analogues for laboratory measurements.

The upcoming observations of the ESA-JAXA-BepiColombo mission (Benkhoff et al., 2021) will provide new datasets allowing the study of the surface of Mercury from the UV to the IR. The Spectrometer and Imaging for MPO BepiColombo Integrated Observatory SYStem (SIMBIO-SYS) (Cremonese et al., 2020) and the Mercury Radiometer and Thermal Infrared Spectrometer (MERTIS) (Hiesinger et al., 2020) will map the surface of Mercury in the VMIR and the effect of SpWe including ion irradiation is a crucial factor for the interpretation of future data. Together these instruments will enable us to gain a deeper understanding of the spatial definition and origin of spectral units on Mercury as well as the mineralogy of the surface. VIHI, the hyperspectral imager of the SIMBIO-SIS payload and MERTIS will map the surface between 0.4-2 µm and 7-14 µm respectively. This study aims to simulate, for the first time, solar wind ion irradiation on Mercury's terrestrial rock analogues (boninite, basaltic komatiite and komatiite) in the VMIR using strong energy and fluences. The main objectives are to characterise the spectral alteration induced by ion irradiation and provide a benchmark understanding of Mercury's surface weathering in preparation for BepiColombo.

2. Terrestrial analogues and Mercury's environment

2.1. Sample characteristics

As no direct information from returned samples is available, we used three terrestrial ultramafic rocks that represent good analogues for Mercury's volcanic surface: a boninite, a basaltic komatiite and a komatiite. Smooth plains on Mercury are often compared to flood basalts and komatiite (Head et al., 2011) that formed the Large Igneous Provinces (LIPs) on Earth. Both the komatiite and the basaltic komatiite come from the Caribbean plateau at Gorgona Island known for its upper cretaceous ultramafic rocks sequence including komatiite (Aitken and Echeverria, 1984; Serrano, 2009; Serrano et al., 2011; Carli et al., 2013). The Gorgona Island is one of the least deformed and most recently accreted pieces of the Caribbean Large Igneous Province (CLIP). The boninite comes from Troodos ophiolitic Massif located on Cyprus island (Mari et al., 2023). The conditions on Mercury vary significantly from what we observe on Earth. Our samples underwent weathering and alteration processes similar to those on Earth, resulting in some spectral characteristics that are unexpected on Mercury (Mari et al., 2013).

Boninite, basalt and komatiite are three high-Mg volcanic rocks. The main differences are based on compositions and textures (spinifex texture for the komatiite: preferential orientation of dendritic olivine or pyroxene crystals). Boninites are defined by MgO > 8 %, TiO_2 < 0.5 % and SiO_2 > 52 % in comparison with komatiites defined by MgO > 18 %, TiO_2 < 1% and 30 < SiO_2 < 52 %. Komatiites have a Na_2O+K_2O < 2 % whereas basalts have a Na_2O+K_2O > 2 % (Le bas, 2000). A basaltic komatiite is compositionally close to a komatiite with a lower MgO and higher SiO_2. Regarding the elemental composition (Table 1) the boninite used in the present work belongs to the low-Si boninite group and the two other samples are well characterised by a basaltic komatiite and a komatiite (Le bas et al., 2000; Pearce and Reagan, 2019).

Elemental composition	Terrestrial analogues (Serrano, 2009; Mari et al., 2023)			Geochemical units from Vander kaaden et al. (2017)						
wt%	Boninite	Basaltic komatiite	Komatiite	CB	NP-LMg	NP-HMg	HMR	HMR-CaS	HAl	IT
$Si0_2$	43.09	49.329	43.350	58.00 (4.75)	58.87 (7.43)	53.44 (7.49)	50.52 (7.04)	49.27 (5.95)	53.94 (4.23)	54.38 (8.05)
TiO_2	0.42	1.370	0.425	0.45	1.38	1.25	1.18	1.15	1.26	1.27

				(0.16)						
Al_2O_3	13.78	13.759	10.846	16.35 (0.97)	11 .79 (2.40)	12.24 (1.51)	9.80 (1.36)	9.04 (1.82)	16.34 (0.57)	13.68 (1.80)
FeO	18.83	10.094	11.330	0.97 (0.21)	1.57 (0.47)	1.97 (0.31)	1.94 (0.51)	2.14 (0.31)	0.94 (0.31)	1.79 (0.34)
MgO	8.82	8.487	19.758	12.86 (2.28)	12.13 (2.84)	19.75 (3.90)	23.54 (2.86)	24.52 (2.32)	16.06 (1.47)	17.46 (4.62)
CaO	11.52	11.246	8.875	5.62 (0.63)	5.27 (1.23)	5.43 (1.20)	6.82 (1.70)	7.57 (1.35)	5.58 (1.59)	5.59 (0.93)
Na_2O		2.746	0.695	3.51 (0.01)	6.47 (0.04)	3.51 (0.01)	3.51 (0.01)	3.51 (0.01)	3.51 (0.01)	3.51 (0.01)
K_2O	1.26	0.196	0.033	0.09 (0.02)	0.18 (0.04)	0.24 (0.04)	0.16 (0.03)	0.16 (0.03)	0.16 (0.03)	0.11 (0.02)
Cr_2O_3	0.27									
MnO	1.59	0.171	0.188	0.70	0.71	0.65	0.61	0.59	0.65	0.66
NiO	0.16									
P_2O_5		0.115	0.037							
CrO				0.71	0.72	0.65	0.62	0.60	0.66	0.66
S				1.50 (0.50)	1.82 (0.49)	1.75 (0.57)	2.60 (0.60)	2.89 (0.29)	1.83 (0.07)	1.76 (0.37)

Table 1: Elemental composition of the terrestrial analogues in comparison with geochemical units on Mercury defined by Vander Kaaden et al. (2017). CB: the interior smooth plains of the Caloris basin, NP-HMg: a subset of the Northern volcanic Plains (NP) with relatively high Mg content, NP-LMg: a subset of the NP with relatively low Mg content, HMR: the high-Mg region, HMR-CaS: a sub-region of the HMR with the planet's highest Ca and S contents. HAl: the high-Al regions. IT: intermediate terranes.

The boninite is composed of orthopyroxene (66.8 wt% enstatite) and olivine (33.1 wt%, forsterite) (Mari et al., 2023). The composition of the basaltic komatiite and the komatiite is slightly more diverse (Serrano, 2009). The basaltic komatiite contains clinopyroxene (23-29 wt%, mainly Mg-rich clinopyroxene), olivine (15-25 wt%), plagioclase (19-27 wt%), volcanic glass (23-26 wt%) and accessory minerals. The komatiite is composed of clinopyroxene (15 wt%, mainly Mg-rich clinopyroxene), olivine (35 wt%), plagioclase (21 wt%), volcanic glass (12 wt%) and accessory minerals.

The MgO differences, and more generally the elemental compositional differences, between the boninite, the basaltic komatiite and the komatiite can be used to investigate the spectral differences between volcanic units on Mercury. We used geochemical units and average compositions defined by Vander Kaaden et al. (2017) to compare our terrestrial analogues with units on Mercury. The SiO_2 values are lower than Mercury's composition, except for the basaltic komatiite, as well as the MgO of the boninite and basaltic komatiite. The lower SiO_2 content indicates that our samples come from a more primitive magma. The boninite and basaltic komatiite reflect the composition of Caloris interior volcanic smooth plains (CB), high-Al regions (HAl) and a part of the Northern Plains lower in MgO (NP-LMg) (Table 1). In comparison, the MgO composition of komatiite is closer to the High Magnesium Region (HMR) and High MgO part of the Northern Plains (NP-HMg). The basaltic komatiite almost coincides with the HMR-CaS region, especially regarding the SiO_2 composition suggesting a reliable analogy even if the MgO content is lower. The IT is the most common geochemical unit on Mercury. The MgO concentration of the IT is closer to the komatiite but the best analogue seems to be the basaltic komatiite according to the SiO_2, and Al_2O_3 contents. The basaltic komatiite is the sample that fits the most units on Mercury in comparison with the boninite and the komatiite.

One of the most distinctive features of Mercury's surface is its low iron content. Earth-based observations (Vilas, 1985; Blewett et al., 2002; Sprague et al., 2002; Warell, 2002), MESSENGER flyby measurements (McClintock et al., 2008) and MESSENGER orbital data (Evans et al., 2012; Izenberg et al., 2014; Weider et al., 2014; Nittler and Weider, 2019; Nittler et al., 2020) have shown that Mercury’s surface contains very little amount of iron in contrast to its high bulk composition. Fe-O bounds in silicates produce a spectral reflectance absorption band at ~ 1µm (Burns, 1993). On Mercury, the global lack of ~ 1µm absorption band indicates that there are only a few percent of FeO in silicates. The exact amount remains controversial and summarised in Domingue et al. (2014), noting for example a FeO maximum abundance of < 1 wt% according to Klima et al. (2013), about 4 wt% by Nittler et al. (2011) and Izenberg et al. (2014) or around 8 wt% according to Warell et al. (2010). Nevertheless, the iron surface composition is heterogeneous and Warell et al. (2006) noticed a shallow absorption band centred at 1.1 µm localised on Mercury (Boynton et al., 2007). The comparison of MESSENGER observations with reflectance models and compositional data suggests that surficial iron has mostly been converted to nanometer-scale metallic iron

particles (called: nanophase reduced iron or submicroscopic iron particle and noted respectively: $npFe^0$ or SMFe) due to SpWe (Noble et al., 2007; Lucey and Riner, 2011; Weider et al., 2014; Trang et al., 2017). These particles bias the determination of available FeO in the crust. With a better spatial resolution and Signal-to-Noise Ratio (SNR) BepiColombo is eagerly awaited to precise the FeO content and spectral signature.

Even if our samples have undergone earthlike weathering and aqueous alteration and even if the FeO compositions are above the estimations for Mercury's surface, they remain reasonable and accessible candidates as natural terrestrial rock analogues. For a good quality comparative analysis with Mercury data, it is important to avoid spectral features that are not observable on the Mercury spectra at this time like the 1 µm absorption band. In addition to the low iron content, SpWe could also explain the absence of features in Mercury's VNIR spectra. We will therefore not make a detailed study of the band, but will briefly discuss the effect of ion irradiation on the lack of features.

2.2. Hermean solar wind conditions

Mercury is surrounded by solar wind, solar wind ions being the major contributors to SpWe on Mercury. Large portions of the surface are exposed to the solar wind because of the lack of a dense atmosphere, the weak internal magnetic field and the strong solar wind environment. Solar wind ions are H^+ and He^{2+} with a weak contribution of heavy elements (Bame et al., 1975). Typically, protons impact Mercury with an energy between $\sim$ 500 eV to $\sim$ 1.5 keV, higher than $\sim$ 1 keV on the Moon. Concerning electrons, they are mostly found in a range of 0.1 to 10 keV (Lavorenti et al., 2023). The energy can reach 10 KeV, with protons and electrons gaining energy at magnetic reconnection when they cross Mercury's cusp (footprints of open magnetic field lines, magnetic lines that have one end connected to the solar wind) regions (Massetti et al., 2007; Lavorenti et al., 2023). High-energy ions are also emitted from the Sun through solar flares and active regions with significant effects on surfaces (Johnson et al., 1990; Brunetto et al., 2014; Matsumoto et al., 2015). In general, the plasma precipitation on Mercury is very heterogeneous (in latitude and longitude) and will mostly depend on solar wind conditions as well as solar wind-magnetosphere interactions (Lavorenti et al., 2023). Typically, a surface of $\sim 10^{12}$-10^{13} m^2 facing the Sun receives a flux of $\sim 1.5 \times 10^{12} - 2 \times 10^{13}$ ions/m^2 s (Killen et al., 2007; Wurz et al., 2010; Massetti et al., 2007;

Lavorenti et al., 2023). The surface of Mercury is exposed to a fluence of ~ 10^{14} protons/cm^2 integrating over two Mercury orbits (176 Earth days) (Lavoreti et al., 2021).

3. Protocols and experimental setups

3.1. Pellets formation

Due to experimental constraints, we performed our analysis on pellets. Pellets simulate an intermediate case between a fine regolith and a rock. A spectrum obtained from a pellet will be bluer than one obtained from a powder of the same composition and grain size (Carli et al., 2013; Vernazza et al., 2013). Mercury's regolith is assumed to be dominated by fine-grained materials but we do not have precise knowledge of the regolith's grain size (Langevin et al., 1997). Terrestrial samples were therefore crushed into powder of grains size ≤ 36 µm, close to an approximation of Mercury's regolith (Sprague et al., 2002; Warell et al., 2010). We acknowledge that pressing the powders into a pellet reduced the surface roughness, the grain size, and both the intra- and inter-granular porosity of the uncompressed powder, however the extent of these possible alterations was not determined. Pellets were prepared at the Institut d'Astrophysique Spatiale (IAS, Orsay, France) by pressing ~ 270 mg of powder using a Specac manual hydraulic press. Each pellet was pressed under 6 tons during 5 minutes. The resulting pellets are 13 mm in diameter, about 1-2 mm thick and homogeneous. The produced pellets are not sufficiently thick and are likely to move in the sample holder during the experiment. To avoid this, we prepared KBr pellets of approximately the same size to place below the sample in the sample holder. KBr pellets were created by pressing 400 mg of KBr at 5 tons for 4 minutes. From the studied material, two pellets each of komatiite, basaltic komatiite and boninite were created for the two experiments outlined in Section 3.2.

3.2. Ion irradiation

Ions of several species and energies are involved in the solar wind irradiation of Mercury's surface. However, due to experimental limitations in time and resources, we decided to focus on He^+ at 20 keV. Irradiations performed in this work are thus not an exhaustive reproduction of solar wind ions reaching Mercury. Hydrogen is the main component (~96%) of solar wind while helium is the second most abundant species (~4%).

Unlike hydrogen, helium ions He^+ are non-reactive, allowing us to avoid complications with implantation-induced chemistry (e.g. Brucato et al., 1997; Liu et al., 2012; Bandfield et al., 2018) making them our first choice for this study. The solar wind is composed mainly of H^+ and He^{2+}, thus the use of He^+ instead of He^{2+} implies a much lower potential sputtering effect (see, e.g. Hijazi et al., 2017; Szabo et al., 2020).

We used an energy of 20 keV (5 keV/amu) similar to those of suprathermal tail and pickup ions, in between the fast solar wind and the low-energy range of solar energetic particles (Mewaldt et al., 2007; Mason et al., 2008). The energy we use (5 keV/amu) is approximately five times greater than the energy of the slow solar wind (∼1 keV/amu). The contribution of high-energy helium ions to SpWe is not negligible and can significantly modify the surface of an airless body (Matsumoto et al., 2015). Moreover, the weathering timescale is longer at high energy than at the average energy of 1-4 keV (Brunetto et al., 2014). The energy of 20 keV is of particular interest as it has been highlighted by Jäggi et al. (2021) that the effect of average solar wind is almost negligible on Mercury analogues. Fluences can be adapted from previous studies based on meteorite and mineral measurements. Experimental studies of SpWe on asteroids with stronger energy (40 keV) and helium ions have shown that a fluence of $< 1 \times 10^{17}$ ions/cm^2 allowed an exponential darkening and reddening of carbonaceous chondrites (Lantz et al., 2017). However, the asymptote indicating a potential saturation was not reached. Furthermore, Chrbolková et al. (2021) have shown only a weak spectral alteration of silicates in the visible at a fluence of 1×10^{17} ions/cm^2, and an energy of 20 keV, due to an insufficient fluence. To try to reach a putative saturation of our samples discernible in spectra we decided to irradiate up to 5×10^{17} ions/cm^2.

Ion irradiations were performed with the SIDONIE electromagnetic isotope separator (Chauvin et al., 2004) (CSNSM, Orsay, France) interfaced with the INGMAR (IrradiatioN de Glaces et Météorites Analysées par Réflectance VIS-IR, IAS-CSNSM, Orsay, France) setup through which in-situ reflectance spectroscopy measurements were done. We used He^+ at 20 keV under vacuum ($P \sim 10^{-7}$ mBar) with the following fluences 1×10^{16}, 3×10^{16}, 6×10^{16}, 1×10^{17} ions/cm2 including a measurement before irradiation. Additional measurements were done in a second irradiation campaign reaching 5×10^{17} ions/cm^2 including several intermediate doses according to the sample. The intermediate doses were not the same for all the samples. We performed measurements before irradiation for each sample. The

irradiated komatiite was measured after fluences of 2.89 x 10^{17} ions/cm^2 and 5 x 10^{17} ions/cm^2; the basaltic komatiite was measured after 3 x 10^{17} ions/cm^2, 4 x 10^{17} ions/cm^2, and 5 x 10^{17} ions/cm^2 finally, concerning the boninite we performed measurements after fluences of 4 x 10^{17} ions/cm^2 and 5 x 10^{17} ions/cm^2. The ion flux was $\sim 10^{13}$ ions/ (cm^2s) on average. For each sample, a part of the pellet (slightly less than half of it) was preserved from irradiation by using a copper mask. This allowed us to keep a piece of pristine material and perform additional measurements later on (especially ex situ in the MIR) to compare before (fresh) and after irradiation spectra.

Unlike asteroids, Mercury is partially and unequally protected by its magnetosphere making it difficult to relate ion irradiation simulations and alteration time scale. For a 20 keV solar wind flux on Mercury, and considering only helium precipitation, the fluences would correspond to an exposure time of ~16 thousand to 8 million years (see Lavorenti et al., 2023 and Raines et al., 2022 for fluxes and energies). The shorter time corresponds to the areas of the surface with the highest precipitation fluxes (and our minimum fluence), while the longer time corresponds to the areas of the surface with the lowest (and our maximal fluence). We would like to point out that these values correspond to a surface irradiated only under our conditions. As Mercury's surface is irradiated by other ions at other energies, the time scale will be shorter. Moreover, this is without taking into account the additional components of SpWe.

3.3. VNIR measurements

Using the INGMAR setup, bidirectional reflectance spectroscopy was performed from the visible (0.4-1.05 µm) to near-infrared (0.9-2.5 µm). Measurements were acquired after each step of irradiation directly in the vacuum chamber at room temperature. Both VIS and NIR measurements were performed on the same spot (Lantz et al., 2017). The illumination spot sizes are 20 mm in the VIS and 12 mm in diameter in the NIR with a collecting spot size of 3-4 mm. In the VIS we used a grating spectrometer (Maya2000Pro, Ocean Optics) with a spectral resolution of 0.5 nm. In the NIR spectra were acquired using a Fourier Transform spectrometer (Tensor37 Bruker) with a spectral resolution of 32 cm^{-1}. Spectra were collected with a fixed emission angle e=15° and i=15° (α=20°) in the VIS in comparison with i=20° (α=15°) in the NIR. To calibrate the absolute reflectance, we used a Spectralon standard (with 99% Lambertian reflectance; Labsphere). There is an offset between the VIS and NIR

spectra mainly due to a geometry effect as well as a slight non-linearity of the detectors. The final spectra presented in this work were corrected by the Spectralon hydration and merged in VNIR final spectra using a region of common wavelengths.

3.4. MIR measurements

MIR measurements, between 2 and 16 µm, were performed ex-situ on the samples after the final irradiation dose. Those analyses were conducted at the Synchrotron SOLEIL (France) using the SMIS beamline (Spectroscopy and Microscopy in the Infrared using Synchrotron) (Dumas et al., 2006). We used a microspectrometer (model Cary 670/620) having its internal Globar light source and a MCT detector cooled with liquid nitrogen. Reference spectra were collected on a gold sample. Measurements were done at ambient temperature using a 15x objective; the spot size was between 160 and 400 μm^2 and the spectral resolution was 4 cm^{-1}. Measurements on the non-irradiated part of each sample were made accurately by removing the copper cover (see 3.2) at the very last moment. Furthermore, the irradiated and non-irradiated sides were identifiable by slight differences in colour. Spectra presented in this work are an average of three to five measurements performed on several areas both for the non-irradiated and irradiated part of each sample. Average spectra allow us to take into account the heterogeneities of the sample in the interpretation. Despite this, certain differences in reflectance intensity may be linked to the choice of the sampled area. To avoid any interpretation bias, we normalised the spectra to the largest peak.

4. Results

4.1. Visible to Near-infrared

We obtained one VNIR spectrum for each sample at each fluence up to $1x10^{17}$ ions/cm^2 (Figure 1 A, C, E). The boninite exhibits a global reflectance that is lower than the basaltic komatiite, which in turn is lower than that of the komatiite. All samples exhibit a broad ~ 1 µm band consistent with mafic mineralogy. Moreover, all samples show hydration bands associated with aqueous alteration at ~ 1.4 µm and ~ 1.9 µm observable for the boninite. Alteration can also explain the minor features at ~ 0.65 - 0.75 µm and ~ 2.2 - 2.4 µm. Globally, the spectral alteration due to ion irradiation is weaker in the NIR. In the VIS we

observe three major alterations of spectroscopic features upon irradiation (Figure 1 B, D, F): a decrease in reflectance (darkening), an increase of the spectral slope with wavelengths (reddening) and a less important curvature in the near-UV to visible (flattening). The absorption band at ~ 1 µm underwent only minor alterations after irradiation. We do not observe any significant shift or distortion of the band. After an irradiation of 1×10^{17} ions/cm^2, the minimum of the band is shifted of ~0.3, 0.02, and 0.005 µm respectively for the boninite, the basaltic komatiite and the komatiite. However, as the main absorption band at ~ 1 µm was not observed yet on Mercury, spectral parameters used in this study are defined outside this absorption band. The irradiation conditions and analogues used in this study do not explain the absence of an absorption band in the VNIR spectra on Mercury. Ion irradiation may not be the main process of reducing spectral band signatures on Mercury (Lavorenti et al., 2023).

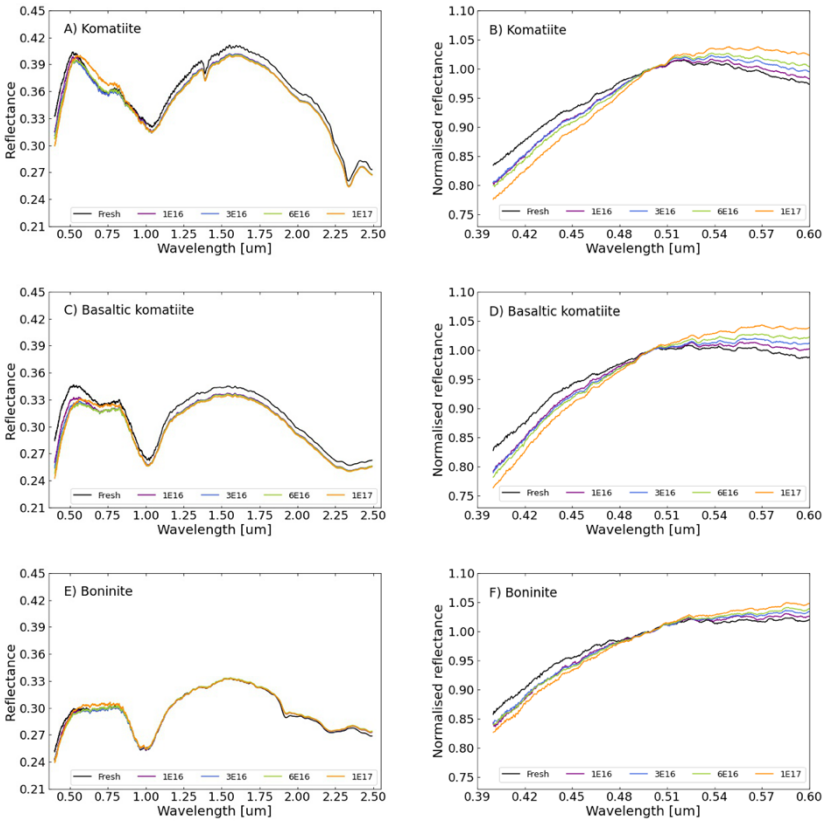

Figure 1: A) C) E) VNIR spectra for the komatiite, basaltic komatiite and boninite respectively according to the fluence up to 1.10^{17} ions/cm^2. B) D) F) Normalised spectra at 0.5 µm. The normalization highlights the slopes and shape of spectra according to the fluence.

Spectral parameters have been defined to constrain the alterations induced by irradiation (Table 2). We used the absolute reflectance at 0.45 µm (R450) as well as the slope (calculated by linear fit) between 0.41 and 0.5 µm (S410-500). An additional parameter (curvature) adapted from Barraud et al. (2020) was used to highlight the curvature alteration on the spectra between 0.41 and 0.5 µm. These spectral parameters have been chosen to avoid the 1 µm absorption band while being close to parameters used in remote sensing data analysis on Mercury (Barraud et al., 2020; Caminiti et al., 2023).

Spectral parameter	Spectral range [µm]	Mathematical expression	Description
R450	0.45	-	Reflectance at 0.45 µm
S410-500	0.41-0.5	Reflectance (λ)=S410*λ+b	Obtained by linear fit
Curvature	0.41-0.5	Reflectance (λ)= curvature*λ^2+bλ+c	Obtained by polynomial fit (degree 2)

Table 2: Parameters used to describe the alteration of spectroscopic features induced by ion irradiation.

After the first irradiation experiment, giving results until 1 x 10^{17}ions/cm^2, and in order to clarify the trends, additional measurements were performed in a second experiment reaching fluences up to 5 x 10^{17} ions/cm^2 (see 3.2). It is worth noting that pellets made from the same fresh material have different initial (before irradiation) reflectance, slope and curvature between the first and second experiments. Any differences in composition between pellets of the same material would not affect the data presented here, due to the large collection area (3-4 mm diameter). The observed difference could stem from variations in crystal orientation and surface morphology of the pellets before ion bombardment. However, these discrepancies do not impact our study as we are focused on analysing relative changes. To facilitate data comparison, we adjusted the results from the second experiment to align with the first one by correcting the offset of fresh samples and applying the offset correction to all the dots obtained during the second experiment.

R450 decreases from the first irradiation dose until 5 x 10^{17} ions/cm^2, showing irradiation-induced exponential darkening (Figure 2A). S410-500 increases with irradiation showing a reddening until 1 x 10^{17} ions/cm^2 (Figure 2B). Unlike the exponential darkening,

the reddening shows no identifiable trend except a global increase with irradiation doses. It is noticeable that the first irradiation dose at 1 x 10^{16} ions/cm^2 is slightly out of phase with the following measurements. Several trends in the reddening can be observed. There is a quick increase in reddening at the lowest doses until 3 x 10^{16} ions/cm^2, followed by a transition with a slowdown in reddening until 6 x 10^{16} ions/cm^2. Finally, we notice a new steep reddening increase going up to 1 x 10^{17} ions/cm^2. Unlike darkening, reddening does not appear to reach a steady state at 1 x 10^{17} ions/cm^2. After an increase until 1 x 10^{17} ions/cm^2, S410-500 seems to stabilise, showing no further identifiable trend with irradiation up to 5 x 10^{17} ions/cm^2 (Figure 2B). The three samples reached a putative plateau and strong irradiation doses even show a S410-500 close to the initial value of the fresh sample. The irradiation modifies the concavity of the spectra between 0.41 and 0.5 µm. This study shows that the curvature (Figure 2C) increases with irradiation leading to a flattening of the spectra. As for S410-500, the first irradiation dose is a bit out of phase. The curvature of the komatiite increases from the fresh sample to 1 x 10^{17} ions/cm^2. However, for the basaltic komatiite and the boninite, we notice an increase of the curvature until 6 x 10^{16} ions/cm^2 and the beginning of stabilisation at higher doses (Figure 2C). Going up to 5 x 10^{17} ions/cm^2, the same type of putative plateau behaviour as for the reddening is observed for the curvature even for the komatiite that had a different behaviour than the two other samples (Figure 2C).

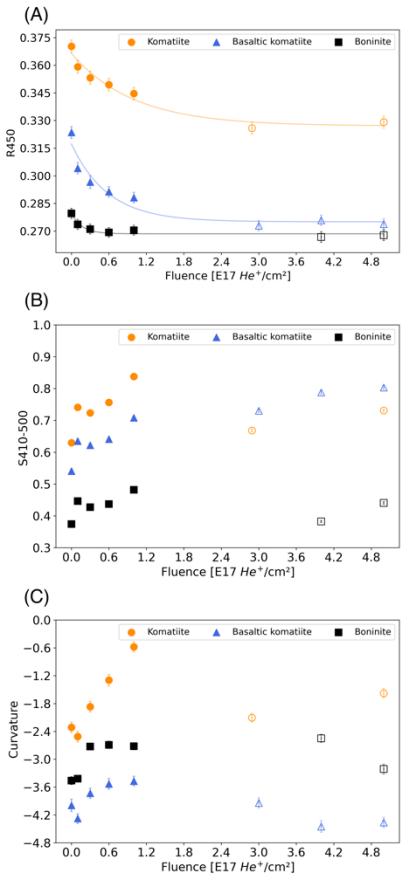

Figure 2: *Evolution of R450, S410-500, and the curvature upon ion irradiation up to 5x10^{17} ions/cm^2. Measurements were done on different pellets from the same material between the first experiment (up to* 1 x 10^{17} ions/cm^2*) and the second one (up to* 5 x 10^{17} ions/cm^2*). Pellets from the same material show different fresh values. This effect does not impact our study as we are focused on relative alteration more than absolute values. To facilitate data comparison, we adjusted the results from the second experiment to align with the first one by correcting the offset of fresh sample and applying the offset correction to all the dots. The error estimated on the reflectance is 1% in relative value for each sample. The error on the spectral slope includes the one on reflectances and the one related to the linear fit. If the error bar is not visible it indicates that it is smaller than the symbol. A) An exponential fit was used to fit the trend of the darkening (y = a + b*exp(x* c)) with a=0.32701211, b=0.03938215, c=-1.0026452 for the komatiite; a= 0.27503765, b=0.04220309, c=-1.71623442 for the basaltic komatiite and a=0.26849724, b=0.0107228, c=-5.77594749 for the boninite. B) Evolution of the spectral slope. C) Evolution of the curvature.*

We propose to focus on the well-defined trends until 1 x 10^{17} ions/cm^2. If we normalise the spectra of each dose by the fresh spectra and calculate R450 on the final spectra (Figure 3A), we see that the intensity of the darkening depends on the sample. The reflectance of the basaltic komatiite is more affected by ion irradiation than the komatiite, itself more altered than the boninite. The decrease in reflectance is 3%, 7% and 11% respectively for boninite, komatiite and basaltic komatiite at 1 x 10^{17} ions/cm^2 where a steady state starts to be reached for the boninite. As for the reflectance, the reddening is more pronounced on the basaltic komatiite than on the komatiite and on the boninite (Figure 3B). The flattening follows a different trend and intensity according to the sample and is more pronounced on the komatiite than on the boninite and on the basaltic komatiite (Figure 3C). It is noticeable that the basaltic komatiite and the boninite have a similar evolution while the komatiite shows its own trend with a stronger flattening (Figure 2C and 3C). As shown in Figure 1, it's worth noting that the absorption band centred at approximately 1 µm begins at a shorter wavelength for komatiite compared to both basaltic komatiite and boninite. This discrepancy can have an impact on the spectral characteristics and could explain the komatiite trend isolated from the two others.

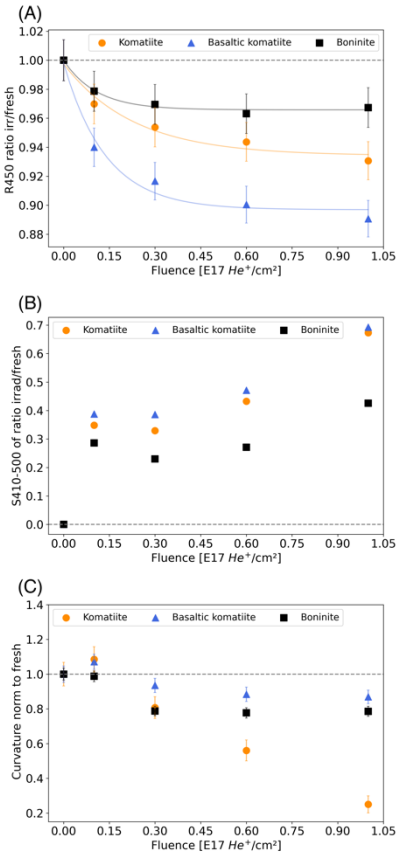

Figure 3: Evolution of R450, S410-500, and the curvature upon ion irradiation up to 5x10^{17} ions/cm^2. R450 and S410-500 are calculated on the ratio of the irradiated and fresh spectra while the curvature is here the ratio of curvature of the fresh spectrum and the irradiated one. *The error estimated on the reflectance is 1% in relative value for each sample. The error on the spectral slope includes the one on reflectances and the one related to the linear fit. If the error bar is not visible it indicates that it is smaller than the symbol. A) An exponential fit was used to fit the trend of the darkening (y = a + b*exp(x* c)) with a=0.93416457, b=0.06327671, c=-4.32889632 for the komatiite; a=0.89691885, b=0.10111709, c=-7.23221054 for the basaltic komatiite and a=0.96578986 , b=0.03405441, c=-9.28290193 for the boninite. The three fresh measurements are overplotted showing only the one of the boninite in the three panels.*

4.2. Effects of composition in the VNIR

The intensity and trends of spectral alterations after irradiation in the VNIR are different according to the sample. The grain size being the same for all powders used in this

study and the collecting spot size being larger than the pellet heterogeneity, we attribute the differences to the composition. There are correlations between R450 and S410-500 (Figure 4) and the SiO_2, TiO_2, FeO and MnO content. Concerning the curvature only one correlation is observable with the MgO content. The darkening and reddening are stronger for the basaltic komatiite than for the komatiite and less pronounced for the boninite. This trend is correlated with a decrease of SiO_2 and TiO_2 (Figure 4A, B) and with an increase of FeO and MnO (Figure 4C, D) from the basaltic komatiite to the boninite. The less SiO_2 and TiO_2 in the sample, the less darkening and reddening. However, the less FeO and MnO in the sample the greater the darkening and reddening. A similar trend is observed for the evolution of R450 and S410-500 according to the SiO_2 and TiO_2 content. A different trend is noticeable for the evolution of R450 and S410-500 according to the FeO and MnO content (Figure 4). FeO and MnO seem to evolve progressively with irradiation. The evolution is coherent and possibly linear. On the other hand, the link between SiO_2 and TiO_2 content is less regular. In fact, we can see that two very close contents will have a very different effect on irradiation, whereas two more distant contents will have a very similar reaction to irradiation. This is even more marked for S410-500 than for reflectance. Concerning the curvature, before 6 x 10^{16} ions/cm^2 there is no correlation between flattening and the composition (Figure 5A). After a certain dose of irradiation, the flattening is more important for the komatiite than the basaltic komatiite than the boninite. This can be correlated with the MgO content (Figure 5B). The less MgO in the sample, the less flattening. Moreover, the MgO content in the basaltic komatiite and the boninite are very close and their trends are very similar. The flattening becomes almost constant after 6 x 10^{16} ions/cm^2 in comparison with the komatiite for which the flattening increases linearly.

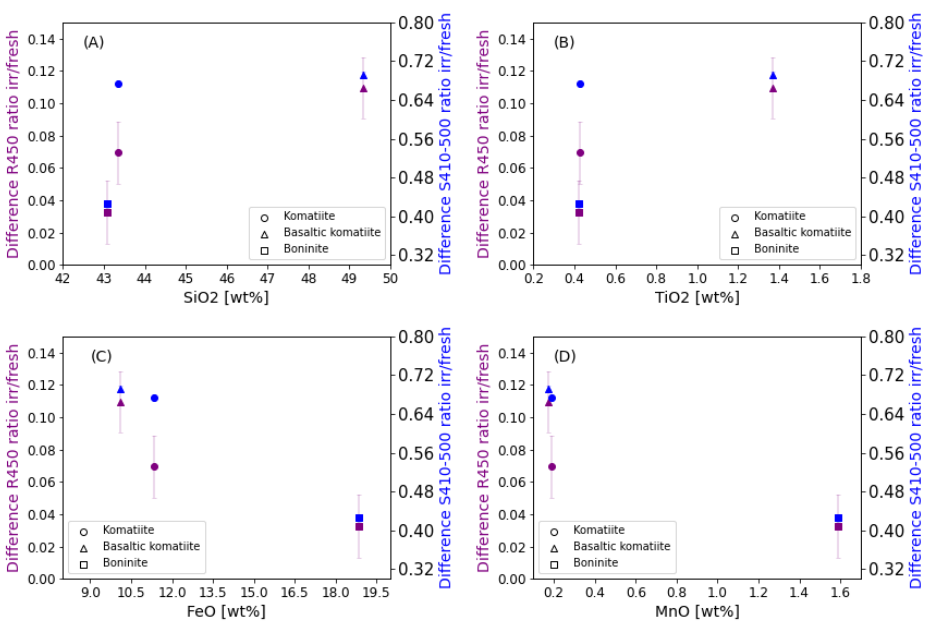

Figure 4: Evolution of R450 and S410-500 according to irradiation at 1×10^{17} *ions/cm²* *and the composition. "Difference" refers to Figure 3A and B the difference between the fresh ratio and the* 1×10^{17} *ions/cm²* *ratio. Here are analysed only the differences between the fresh ratio and* 1×10^{17} *ions/cm²* *ratio. The maximal fluence at* 5×10^{17} *ions/cm2 is not considered in order to study the evolution of spectral parameters before saturation. The intensity of the darkening and reddening is more pronounced for the basaltic komatiite followed by the komatiite and the boninite, correlating with the composition in* SiO_2, TiO_2, *FeO and MnO (Table 1).*

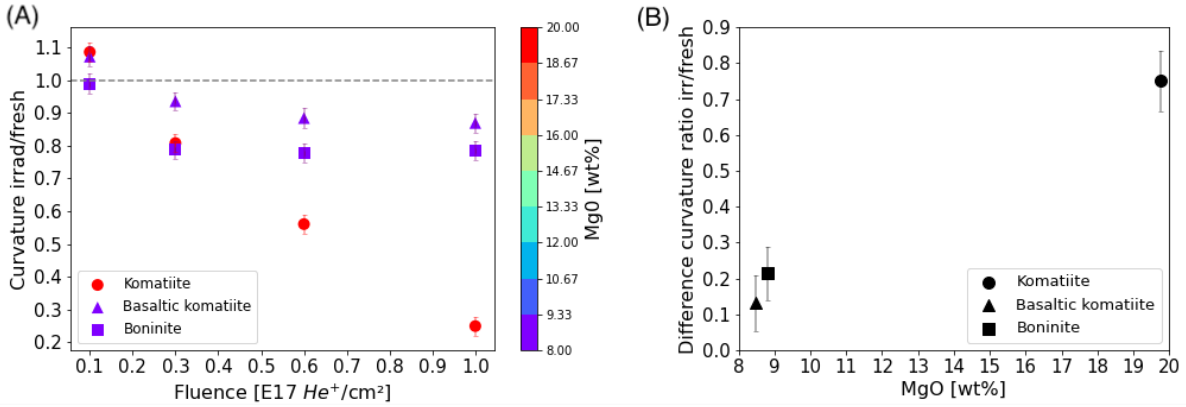

Figure 5: Evolution of curvature according to the amount of MgO and irradiation A) Evolution of the curvature upon ion irradiation until 1 x 10^{17} ions/cm^2 and the MgO content. B) "Difference" refers to Figure 3C the difference between the fresh and irradiated 1 x 10^{17} ions/cm^2 ratio measurement. The intensity of the flattening depends on the MgO content. The flattening is increasingly marked between the basaltic komatiite and the komatiite. The higher the MgO content, the greater the flattening. Here are analysed only the differences between the fresh ratio and 1 x 10^{17} ions/cm^2 ratio. The maximal fluence at 5 x 10^{17} ions/cm^2 is not considered in order to study the evolution of spectral parameters before saturation.

4.3. Mid-infrared

Although MIR range is dominated by silicate features, variations in composition among the samples result in differences in their band shapes, widths and positions (Figure 6). We focus on the Christiansen feature (CF) around 8.5 µm and the Reststrahlen bands (RBs) between 8.5 and 12 µm (Salisbury et al., 1991). The CF is an IR reflectance minimum resulting from a rapid change in the refractive index shortward of the fundamental molecular vibration bands. The RBs stem from fundamental molecular vibration bands due to Si-O stretching and bending motions. We are interested in irradiation-induced alterations of the main RB around 10 µm where there is a strong surface scattering, the CF and an additional second RB between 10 and 12 µm. For the three samples, we observe a widening of the RBs induced by irradiation as well as shifts of RBs and CF (Figure 6). We discuss first the band identification before irradiation.

The boninite spectrum (Figure 6) is the less complex in shape because the composition is only pyroxene and olivine. Additional minerals like plagioclase feldspar add features in the spectra of the basaltic komatiite and the komatiite. The boninite shows a main RB at 9.6 µm and a second one around 11.3 µm (Table 3). We attribute the main RB to the pyroxene (enstatite), and the second RB to olivine (forsterite). Considering the basaltic komatiite (Figure 6), the main RB around 10 µm shows the presence of pyroxene (here probably Mg-rich pyroxene as diopside) and the second RB at 11.4 µm is related to olivine (Table 3). Additional minor peaks are attributed to plagioclase. Finally, the komatiite has a very similar composition to the basaltic komatiite but contains more olivine than pyroxene which could explain the difference in intensity between the RB around 9.8 µm and the second RB just

640 before 11 µm compared to other samples (Figure 6). One has to note that the presence of
641 volcanic glass can reduce the spectral contrast of bands. For example, absorption bands
642 weaken and broaden as the glass content increases in feldspars (Nash and Salisbury, 1991).
643 As we are working with scaled spectra, the presence of glass in basaltic komatiite and
644 komatiite can only result in a broadening of the bands. In our data this is effectively what we
645 observe with broader RBs for the basaltic komatiite (23-26 wt% of glass) than for the
646 komatiite (12 wt% of glass), resulting in a less marked separation between the two RBs of
647 the basaltic komatiite. Indeed, we evaluated the width of the main feature at 60% of its
648 height and found values of ~2.75 µm for the fresh basaltic komatiite (average of the two
649 fresh samples) whereas it is ~1.5 µm for the komatiite.
650

Sample	Irradiation dose [ions/cm^2] and shift	Main RB ~ 10 µm [µm]	CF [µm]	Second RB ~ 11 µm [µm]
Boninite	Fresh	9.62 ± 0.01	8.11 ± 0.01	11.32± 0.01
	1 x 10^{17}	9.78 ± 0.01	8.13 ± 0.01	11.40± 0.01
	Shift at 1 x 10^{17}	0.16	0.012	0.07
	Fresh bis	9.66± 0.01	8.20 ± 0.01	11.40± 0.01
	5 x 10^{17}	9.77 ± 0.01	8.06 ± 0.01	11.42± 0.01
	Shift at 5 x 10^{17}	0.11	-0.14	0.025
Basaltic komatiite	Fresh	9.97 ± 0.01	8.04 ± 0.01	11.43± 0.02
	1 x 10^{17}	10.11 ± 0.01	8.08 ± 0.01	11.58± 0.02
	Shift at 1 x 10^{17}	0.14	0.040	0.15

	Fresh bis	9.97 ± 0.01	8.15 ± 0.01	11.42± 0.01
	5 x 10^{17}	10.39 ± 0.01	8.11 ± 0.01	11.52± 0.01
	Shift at 5 x 10^{17}	0.42	-0.040	0.10
Komatiite	Fresh	9.80± 0.01	8.20 ± 0.01	10.75± 0.02
	1 x 10^{17}	9.99± 0.01	8.40 ± 0.01	10.78± 0.01
	Shift at 1 x 10^{17}	0.19	0.20	0.03
	Fresh bis	9.78± 0.01	8.42 ± 0.01	10.74± 0.02
	5 x 10^{17}	9.99± 0.01	8.24 ± 0.01	10.76± 0.01
	Shift at 5 x 10^{17}	0.21	-0.18	0.02

Table 3: Compilation of the main MIR features position before and after irradiation and the associated shifts. Positions are evaluated as local maxima (RBs) or minima (CF). Fresh values and fresh bis values correspond to the measurement before irradiation on the same powder but two different pellets studied during irradiation experiments one and two respectively (see 3.2). Negative values indicate a shift towards shorter wavelengths (blue-shift) while positive ones a shift towards longer wavelengths (red-shift).

After irradiation, all samples show a shift of the main RB peak at ~ 10 µm towards higher wavelengths (red-shift) with a maximum shift of 0.42 µm for the basaltic komatiite after an irradiation of 1 x 10^{17} ions/cm^2 (see Figure 6 and Table 3 where all values discussed here are compiled). Concerning the CF at ~ 8.5 µm, this work highlights two different behaviours according to the irradiation dose (Figure 6 and Table 3). At 1 x 10^{17} ions/cm^2 the CF is red-shifted while it is shifted toward shorter wavelengths (blue-shifted) at 5 x 10^{17} ions/cm^2. The maximum shifts after irradiation happens for the komatiite with values of +0.20 µm at 1 x

665 10^{17} ions/cm and -0.18 µm at 5 x 10^{17} ions/cm^2 both for the komatiite. We also investigate
666 the second RB between 10 and 12 µm (Figure 6 and Table 3). In general, the red-shift is less
667 pronounced than for the main Si-O peak, in agreement with what was observed by Brunetto
668 et al. 2014 (see this paper for a discussion on this phenomenon, beyond of the scope of the
669 current study), with a maximum shift of 0.15 µm for the basaltic komatiite after an
670 irradiation of 1 x 10^{17} ions/cm^2. We also emphasize here that the komatiite has a very
671 different spectral shape after both irradiation, with the secondary RB becoming the
672 maximum. We observe here a change in band intensity as already seen by Brunetto et al.
673 (2014 ; 2020) and Lantz et al. (2017, in press).
674
675
676
677
678
679
680
681

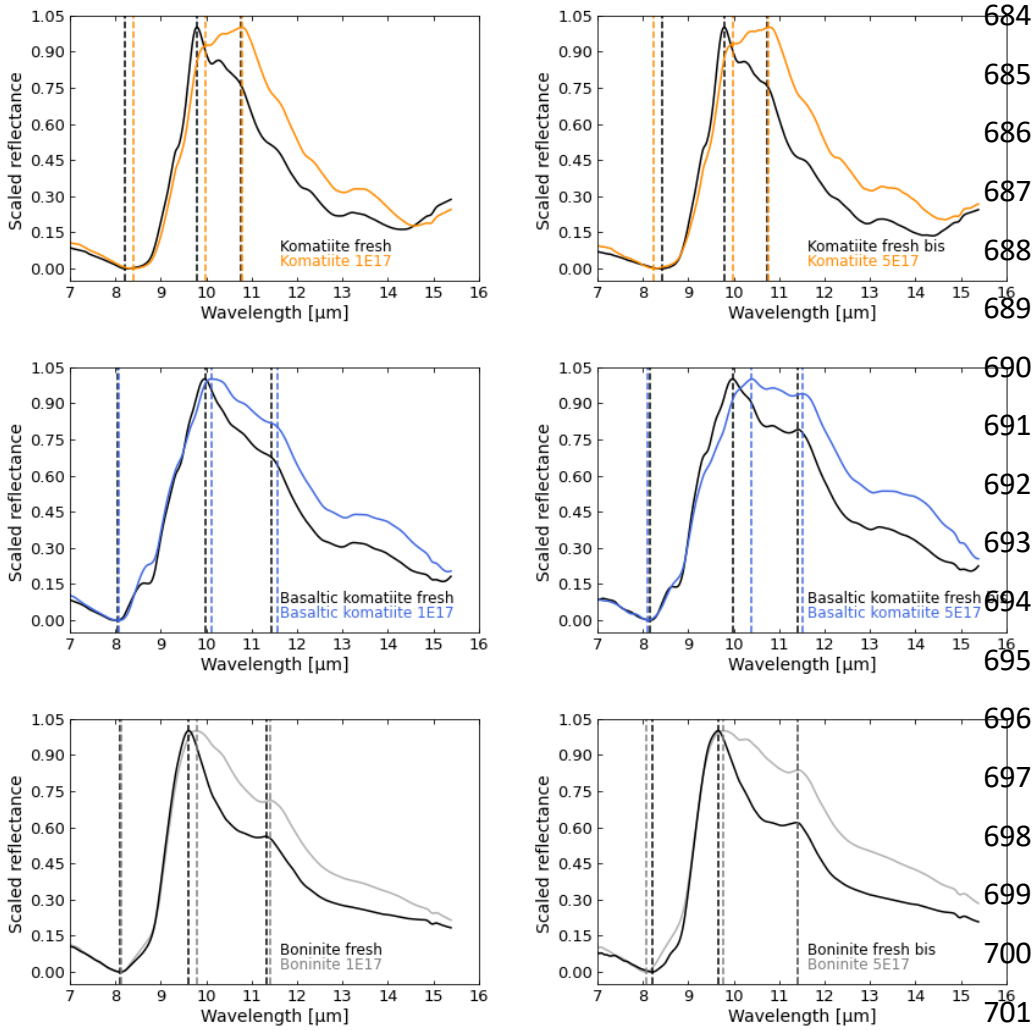

Figure 6: Mid-infrared reflectance spectra of the boninite, the basaltic komatiite and the komatiite. Spectra are scaled at the strongest peak. Irradiation doses are given in ions/cm^2. The left-hand column corresponds to the first experiment and the right-hand column corresponds to the second experiment (same notations as in Table 3).

We observed a broadening of the bands after irradiations for the three samples (Figure 6). For example, the width at 60% of the RB height for the komatiite is increased by ~0.5 µm between the fresh sample and 1 x 10^{17} ions/cm^2, and by ~1 µm after 5 x 10^{17} ions/cm^2.

We decided to analyse our result in a two-component-size space (Figure 7) commonly used to sort measurements and have already proved their effectiveness in

classifying meteorites (Dionnet et al., 2022; Lantz et al., in press). The first thing to notice is that the fresh samples are well separated due to their different initial compositions.

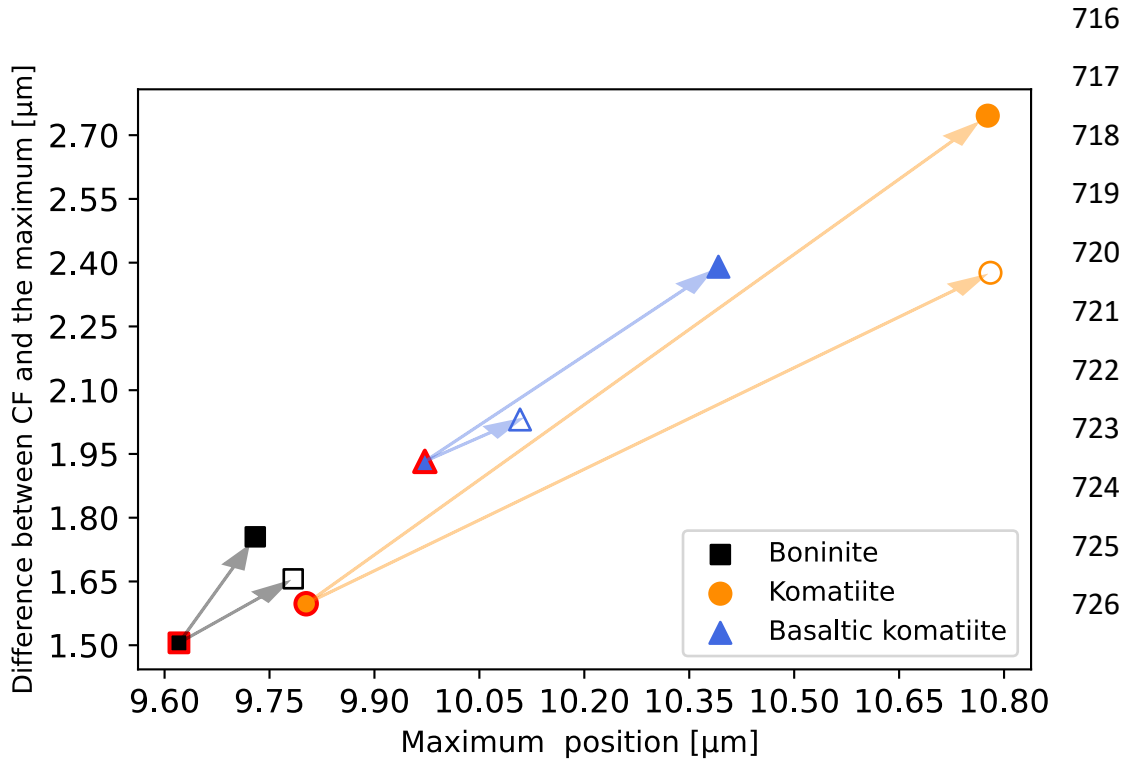

Figure 7: Evolution of the position of the maximum reflectance according to the difference between the CF and the position of the maximum reflectance. For each sample there are fresh samples in full symbols with red edges, linked to two other dots, the open being 1 x 10^{17} ions/cm^2 and the full one 5 x 10^{17} ions/cm^2. As measurements were done on the same powders but different pellets there is a difference between fresh measurements before 1x10^{17} ions/cm^2 and 5x10^{17} ions/cm^2. This effect does not impact our study as we are focused on relative alterations more than absolute values. To facilitate data comparison, we adjusted the results from the second experiment (up to 5x10^{17} ions/cm^2) to align with the first one (up to 1x10^{17} ions/cm^2) by correcting the offset of fresh sample and applying this offset to the irradiated sample (same process as Figure 2).

All samples follow the same trend of maximum position redshift upon irradiation for both experiments. The shape of the komatiite spectrum is strongly modified upon irradiation (Figure 6), shifting the maximum of the spectrum towards the longest wavelengths at the level of the second RB. This intense modification of the spectrum is responsible for the longer vectors compared with the boninite and the basaltic komatiite. This difference

743 specific to komatiite could be explained by the composition or by the fact that one
744 component may have been more affected by irradiation, resulting in this change in shape.
745 The particular alteration of the komatiite could be due to olivine. The komatiite is the richest
746 sample in olivine, a mineral that is very sensitive to SpWe (Fu et al., 2012). While the
747 boninite and komatiite seem to have reached their maximum shift already at 1 x 10^{17}
748 ions/cm^2, the highest irradiation produces a bigger shift on the basaltic komatiite. It is likely
749 that these differences are linked to the composition of the samples and is in line with VNIR
750 results showing that the basaltic komatiite is more altered by the irradiation. Furthermore,
751 there is a bigger effect on the y-parameter of this plot after the highest irradiation. Finally,
752 there seems to be a common trend among all samples after the highest irradiation defining a
753 "vector" of SpWe as all arrows become aligned. The steepness of that vector varies between
754 each rock: steeper for the komatiite than for the boninite and the basaltic komatiite. Thus,
755 the steepness of the vector follows the initial composition in MgO and these results could
756 help to constrain the MgO content of different rocks under the same ion irradiation. We
757 highlight here that the distance between the CF and the maximum is a good indicator of
758 SpWe (as proposed by Lantz et al., in press). Together with the maximum position they
759 define a SpWe vector whose inclination helps to relatively compare the irradiation level.
760 When MERTIS data will be available this kind of plot will help in understanding the effect of
761 the environment on remote sensing data, both for composition and SpWe effects.

762 # 5. Discussion

763 ## 5.1. Global darkening and reddening

764 The reflectance and slope in the VIS constitute reliable spectral proxies of irradiation
765 on volcanic surfaces. Even if the carbon content and grain size have a significant effect on
766 spectral properties (Bruschini et al., 2022), SpWe is suggested to be the major contributor to
767 albedo variations on Mercury (Riner and Lucey, 2012). Riner and Lucey (2012) applied a
768 space weathering model to multispectral images of Mercury. They have shown that albedo
769 variations on Mercury cannot be explained by composition or grain size alone but can be
770 explained by the presence of SMFe (influenced by both exposure time to SpWe and
771 composition).

772 The present study confirms the well-known effects, darkening and reddening, of ion
773 irradiation on silicates (Brunetto and Strazulla, 2005; Fu et al., 2012; Loeffler et al., 2009;

774 Chrbolková et al., 2021). These spectral alterations on silicates have been linked to the
775 formation of SMFe (Hapke, 2001; Carrez et al., 2002; Noble et al., 2007; Loeffler et al., 2009;
776 Lucey and Riner, 2011; Pieters and Noble, 2016; Penttilä et al., 2020) due to solar wind
777 implantation. In comparison to the Moon and according to the low amount of available iron
778 on Mercury it is likely that, if there was more iron available in the past, a major part of it has
779 been processed into SMFe by SpWe. Even low concentrations of SMFe (0.02 wt% Noble et
780 al., 2007) can influence surface reflectance properties (Noble et al., 2001, 2007; Loeffler et
781 al., 2009). On Mercury, Lucey and Rinner (2011) have shown that reduced metallic iron could
782 be around 3.5 wt%, more than enough to influence the spectral properties of the surface.
783 This phenomenon is usually accompanied by an amorphization of the target depending on
784 the fluence (Demyk et al., 2001; Carrez et al., 2002; Brucato et al., 2004; Brunetto et
785 Strazulla, 2005). Ion irradiation induces gas implantation which leads to vesiculation (Rubino
786 et al., 2024). The darkening in the visible spectral range could then also be linked to the
787 increase in porosity of the sample surface due to ion implantation (Sultana et al., 2021).
788 Reddening and darkening process in the VNIR does not remarkably affect the mafic
789 silicate absorption feature (Brunetto et al., 2006, Loeffler et al., 2009). We confirm here that
790 there is no significant shift of band position (Brunetto et Strazulla, 2005; Marchi et al., 2005)
791 showing that variations due to chemical compositions dominate ion irradiation spectral
792 alterations (Fu et al., 2012). Mercury spectral units show an evolution from dark material
793 with a shallow slope to bright material with a steeper slope (Robinson et al., 2008; Denevi et
794 al., 2009; Ernst et al., 2010; Murchie et al., 2015; Barraud et al., 2020). Our results confirm
795 experimentally the darkening induced by SpWe through time. In addition, our study is in
796 agreement with observations of Mercury, where the reddening that accompanies darkening
797 is absent after a certain exposure time. We propose two hypotheses to explain this
798 darkening with no reddening:

799 1) The formation of Britt–Pieters [>50 nm SMFe (Lucey and Noble, 2008)] particles
800 causes darkening with no reddening of the surface. Spectral effects of SMFe are different
801 according to the concentration and particle sizes (Noble et al., 2007; Penttil̈a et al., 2020).
802 Different types of SMFe have been identified including “nanophase particles” that both
803 darken and redden the surface and larger “Britt–Pieters particles” that only darken (Noble et
804 al., 2007; Lucey and Riner, 2011; Trang et al., 2017; Penttil̈a et al., 2020). On Mercury, we

expect larger SMFe than on the Moon (Noble and Pieters, 2003). High-velocity impacts on Mercury produce more melt and vapour, moreover, we expect more agglutinates leading to a growth of metallic iron particles (Lucey and Riner, 2011). The high tempera- ture on Mercury's surface will help the Ostwald ripening process (Noble and Pieters, 2003; Deutsch et al., 2024), a mechanism that participates in the coalescence and growth of SMFe. On the 3.5 wt% of SMFe predicted by Lucey and Riner (2011), 3 wt% constitute Britt–Pieters particles. They are at the origin of a darkening with no reddening of the surface.

2) It is possible that the reddening of a heavily space-weathered volcanic surface becomes solar wind flux independent with time. We show that after a certain dose of irradiation, the reddening is no longer observable with values that can be close to the value of the fresh sample. On Mercury, after billions of years of irradiation, it is possible that the slope becomes independent from irradiation.

5.2. Relation between near-UV features and SpWe

This work highlights the flattening of spectra in the near-UV due to ion irradiation. We discussed the link between the Fe content and the spectral property in the visible (see 2.1 and 5.1) but Fe can also modify spectra in the near-UV. MESSENGER reflectance spectra exhibit a downturn from the VIS to the near-UV often used to characterise the surface through several spectral parameters (Goudge et al., 2014; Barraud et al., 2020). This feature in the near-UV can be attributed to Oxygen-Metal Charge Transfer (OMCT) (Bruns et al., 1993; McClintock et al., 2008) and is mainly associated with younger surfaces (Izenberg et al., 2014). Indeed, matured material shows a globally lower albedo and a less curved continuum (McClintock et al., 2008; Robinson et al., 2008; Blewett et al., 2009; Domingue et al., 2014; Murchie et al., 2015; Pieters and Noble, 2016). This preponderance is attributed to the transformation of FeO to SMFe that is more advanced in mature regions (Noble et al., 2007; Lucey and Riner, 2011; Riner and Lucey, 2012; Pieters and Noble, 2016).

Barraud et al. (2020; 2023) support the idea that sulphides are at the origin of the near-UV to VIS curvature observed in hollows. However, the samples used in this work do not contain any sulphide showing that in addition to the composition, the curvature is also influenced by SpWe. This observation emphasises that the shape of the spectra in the near-UV to VIS can bring information on the maturity of surfaces. The curvature can be used with

confidence only for fresh surfaces as the tendency is unclear after 1 x 10^{17} ions/cm^2 with the energy used in this study. Hollows, younger than ~100 thousand years (Wang et al., 2020), are good candidates to explore the variability of the curvature on Mercury according to ion irradiation. We experimentally validate that the near-UV features are, to a certain extent, controlled by solar wind ions irradiation and reflect the soil maturity for the younger surfaces having the same composition which makes it a reliable spectral proxy of irradiation.

5.3. Influence of the composition on spectral properties

We confirmed in this work that under the same conditions, different compositions in silicates show a different sensitivity to SpWe even if they all show a global darkening and reddening until 1x10^{17} ions/cm^2 (Fu et al., 2012; Chrbolková et al., 2021). The present results imply a putative diversity of SpWe on Mercury according to the geochemical terranes.

By comparing olivine, plagioclase and basaltic glass Fu et al. (2012) have shown that olivine is the most sensitive to darkening followed by plagioclase and then basaltic glass. Moreover, olivine is more impacted by reddening than pyroxene (Marchi et al., 2005; Strazzulla et al., 2005; Brunetto et al., 2006, Chrbolková et al., 2021). The curvature follows this trend with a curvature alteration intensity decreasing from the komatiite to the basaltic komatiite where the content in olivine decreases. The curvature is also led by Mg content and a putative preferential sputtering (see 5.4). In fact, the boninite and basaltic komatiite have a very similar content in Mg while the komatiite contains more than twice the amount of Mg. The intensity of the alteration of the curvature after irradiation is very similar for the basaltic komatiite in comparison with the komatiite. However, the darkening and reddening do not follow this tendency concerning olivine. The boninite is dominated by pyroxene (66.8 wt%) (Mari et al., 2023) which could explain the weaker intensity of darkening and reddening in comparison with the basaltic komatiite and the komatiite that are more balanced (Chrbolková et al., 2021).

Variations in reflectance and spectral slope on Mercury do not appear to be directly linked to variations in Fe content. Fe concentration can only play a minor role in surface variation across Mercury (Weider et al., 2014). Nevertheless, by analysing individual mechanisms (darkening mineral content, SpWe, effect of grain size, etc.) Fe content seems to be a key parameter to be taken into account to clarify spectral variation on Mercury. Bruschini et al. (2022) have shown that the amount of iron in silicates influences the

alterations of the spectral slope to graphite content. Silicates containing lower iron content are characterised by a greater alteration in spectral slope versus graphite content. Our study confirms the strong influence of iron content on spectral alterations. The less iron the sample contains, the more sensitive it is to darkening and reddening induced by irradiation. Moreover, Maturilli et al. (2014) have shown that a synthetic analogue with less iron was the most strongly altered after thermal processing, highlighting the importance of iron in spectral alteration induced by the extreme environment. These observations are crucial for the surface of Mercury. As we expect a very low iron content, the effect of darkening and reddening induced by solar wind may be stronger than what is expected (Bruschini et al., 2022).

On Mercury, geochemical units will react differently to SpWe. The Caloris basin (CB column in Table 1) has a high SiO_2 content and a low FeO content in comparison with other units making it one of the most sensitive units to SpWe. The Northern Plains are compositionally heterogeneous (Table 1) and will therefore have a non-uniform SpWe effect that will intensify spectral differences. It is likely that the HMR will be more sensitive to curvature alteration than other units making the flattening more important. Moreover, the HRM, as the NP, shows different sub-area according to the composition that will increase spectral heterogeneities in the region. Mn and Ti are minor elements and it is unlikely that they have a major influence.

5.4. Mid-infrared

Based on laboratory evidence of MIR spectral alteration upon irradiation, we explored the possibility of detecting the irradiation effect through the future remote sensing observation of MERTIS, using band shifts as proxies. Indeed, shifts of the main RB and a part of the shifts of the second RB and CF are higher than the MERTIS spectral resolution of 90 nm. As comparisons with data from Mercury's surface are currently limited in this wavelength range, MERTIS data are expected to be used for comparison with this study.

In the MIR, we observe a red-shift of the RBs positions induced by He^+ irradiation. Amorphization and Mg loss have been proposed to explain the red-shift of Si-O stretching around 10 μm. The volatile Mg could be easily sputtered leading to a loss of magnesium after irradiation (Brunetto et al., 2014; Lantz et al., 2015; 2017) possibly leading to amorphization (Brucato et al., 2004; Demyk et al., 2001; Brunetto et al., 2014). Irradiation

experiments on olivine demonstrated chemical changes including a decrease in Mg/Si ratio supporting this theory (Demyk et al., 2001; Carrez et al., 2002). Some similar shifts have been found with no relation to the elemental composition. Dukes et al. (2015) did not observe a reduction in Mg content after ion irradiation of the Tagish Lake meteorite. Moreover, Rubino et al. (2024) have shown that Mg depletion is not systematic in irradiated samples. So, changes in composition alone do not with certainty explain the observed MIR shifts. The shifts may be caused by the amorphization of the silicates (Brucato et al., 2004; Vernazza et al., 2013). Disorder of the mineral crystal lattice could lead to Si-O stretching feature alteration. Ion implantation appears to preferentially sputter Mg during the amorphization process. However, the sputtered Mg does not necessarily escape from the sample but could remain trapped inside the bubbles produced by vesiculation during amorphization of the sample (Rubino et al., 2024). Thus, the amorphization is not necessarily accompanied by a change in chemical composition (Jäger et al., 2003). Taking into account the composition of our samples and fluences used in this work, it is likely that ion irradiation induced an amorphization and preferential sputtering of Mg, with or without chemical alteration, at the origin of the MIR red-shifts (Demyk et al., 2001; Carrez et al., 2002; Brucato et al., 2004; Brunetto et al., 2014, 2020). We notice that both the main and second RB shifts between fresh and 1 x 10^{17} ions/cm^2 samples are correlated with the MgO content in the fresh sample (Figure A1: A, F). However, for an irradiation of 5 x 10^{17} ions/cm^2 the RBs at ~10 μm shifts are correlated with SiO_2, $Ti0_2$, FeO and MnO while the minor RBs still follow the MgO content (Figure A1: B, C, D, E, G). The correlation between the SiO_2 content and the strongest RB positions is discussed in the case of Mercury analogues in Morlok et al. (2017, 2019, 2021). Here we confirm a correlation between the RB at ~10 μm position and SiO_2. In our case, we observe that higher SiO_2 content is correlated with higher wavelengths of main RB positions. SpWe does not modify this trend.

We observe that in general, the shift is stronger for the intense peak around 10 μm than for the less pronounced feature between 10 and 12 μm showing that the SpWe effect is wavelength dependent. The more intense the band is, the higher the red-shift (Brunetto et al., 2014; Lantz et al., 2017). The strongest absorption bands probe a thinner depth in the sample than low absorption bands and thus are more sensitive to the irradiated surface layer. Photons emerging from the smaller bands come from a deeper layer not significantly modified by irradiation leading to weaker alterations. These shifts do not conflict with the

putative SMFe formation (Hapke, 2001) and show that different bands provide different proxies of irradiation processes by probing different surface layers.

The Christiansen feature depends on the mineralogical composition. Thus, the CF position is expected to be linked to the RB displacement (Brunetto et al., 2020). Our study confirms this trend until 1 x 10^{17} ions/cm^2. However, the CF alterations are not unique and show a different behaviour with a blue-shift after 5 x 10^{17} ions/cm^2. An idea could be that amorphization due to irradiation modifies the CF behaviour. Chrbolková et al. (2021) showed that after irradiation, the olivine CF is red-shifted while the pyroxene CF is blue shifted. We suggest that the olivine being more sensitive to space weathering it will lead spectral alteration until 1x10^{17} ions/cm^2 showing a red-shift while after an intense alteration, pyroxene will dominate showing a blue-shift at 5x10^{17} ions/cm^2. In fresh samples, until 5 x 10^{17} ions/cm^2 we do not see any correlation between CF and SiO_2 content (Morlok et al., 2017; 2019; 2021). We notice a correlation between the CF shift and CaO, K_2O and Al_2O3 content until 1 x 10^{17} ions/cm^2 (Figure A1: H, I, J) though the trend changes after 5 x 10^{17} ions/cm^2 showing a correlation with MgO (Figure A1: K).

The widening of bands is possibly linked with amorphization although chemical alterations are not negligible. The deformation of the bands after irradiation comes from the variation of the relative intensity of the peaks according to the composition. In addition, alterations of the area and wideness of the band can be related to the disordering of the mineral crystal lattice and alterations in composition.

6. Conclusion

Mercury's surface has been space-weathered over time, complicating the interpretation of data derived from remote sensing observations. We presented the first VMIR reflectance spectra of three terrestrial analogues: a boninite, a basaltic komatiite and a komatiite after simulating solar wind irradiation under Mercury's conditions. We used 20 KeV He^+ with fluences up to 5 x 10^{17} ions/cm^2.

- Ion irradiation leads to an exponential darkening of the spectra in the VNIR. The darkening is confirmed by looking at spectral units defined on Mercury with older units being darker than the younger ones.

- Ion irradiation leads to a reddening and flattening of the spectra in the near-UV to the visible. After an irradiation of 1 x 10^{17} ions/cm2 under the conditions of this study, the reddening and flattening stop increasing showing ambiguous trends. Looking at spectral units defined on Mercury, the reddening does not necessarily increase with time. Submicroscopic Britt–Pieters metallic-iron particles could explain this darkening with no reddening. The differences in curvature between spectral units on Mercury are reliable proxies for the alteration of the youngest units.

- The intensity of spectral alterations induced by ion irradiation depends on the composition of the surface. SpWe as well as composition participate in the spectral heterogeneities of the surface of Mercury. We suggest that the FeO, SiO_2, MgO and of less importance TiO and MnO contents can influence the intensity of alterations induced by solar wind in the VMIR. As well as Al_2O3, CaO and of less importance K_2O in the MIR. Mercury's low iron content certainly increases spectral alterations induced by solar wind.

- In the MIR, we detected a consistent red-shift of the RBs induced by ion irradiation. The higher the peak, the greater the red-shift after irradiation. However, shifts of the CF depend on the irradiation dose. RBs and CF shifts represent reliable proxies to detect irradiation effects through future MERTIS observations.

Even if ion irradiation may not be the main process of reducing spectral band signatures on Mercury, the BepiColombo observations are eagerly awaited to provide a better understanding of the absence/weakness of absorption bands in the VNIR. If the rocks on Mercury's surface are comparable to our current terrestrial analogues, it is conceivable that BepiColombo will detect spectral features comparable to those in this study. Waiting for BepiColombo, our work in the VNIR can be used to better understand MESSENGER data. The terrestrial alteration detected in these samples is not expected on Mercury’s surface. Moreover, it is important to note that this study simulates only partly the SpWe effects on Mercury’s surface and additional work should be done to understand the cumulative effects of processes happening in this extreme environment.

Acknowledgments

The authors acknowledge the Centre National d'Etudes Spatiales (CNES) for continuous and long-term support. We also acknowledge the Domaine d'Intérêt Majeur en Astrophysique et Conditions d'Apparition de la Vie+ (DIM ACAV+), île de France, for their support. This research is part of a joint IAS-CSNSM project (INGMAR) and we warmly thank O.Mivumbi and engineers for their help on IGNMAR. This work is part of a LESIA-IAS collaboration and the preparation of the ESA-JAXA BepiColombo mission. Emma Caminiti warmly thanks Aleksandra Stojic for reading this work and providing helpful advice. The authors acknowledge Noah Jäggi and the anonymous referee for their helpful comments at the review stage.

Appendix A: Supplementary figures to support MIR discussion

We present here 11 panels showing the link between the composition and the alteration of MIR features. This figure is a visual representation of correlations between Table 1 and Table 3. Only the correlations mentioned in the text are shown. MIR features showing no correlation with the composition are not represented.

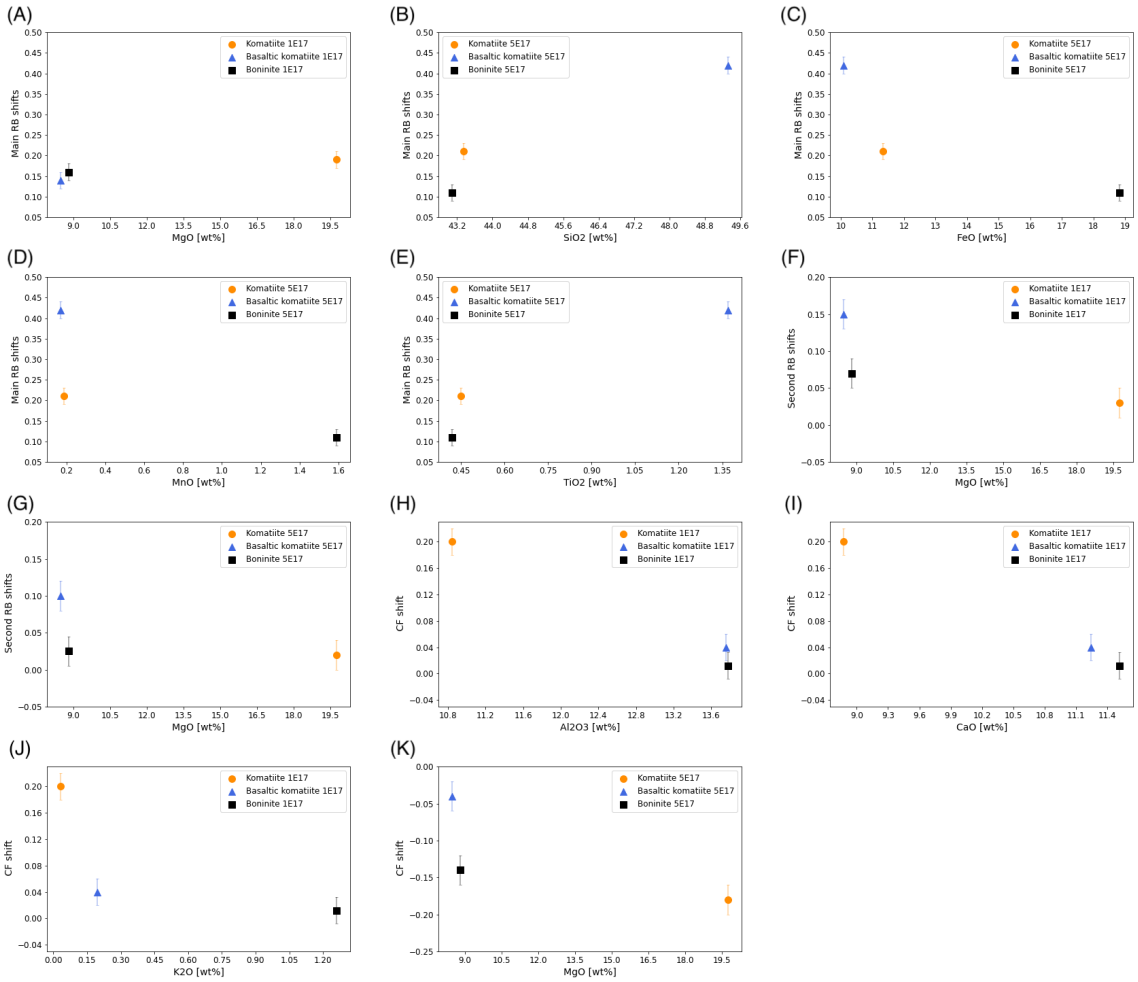

Figure A1: Alteration of MIR features according to the composition.

References

Aitken, B. G., & Echeverría, L. M. (1984). Petrology and geochemistry of komatiites and tholeiites from Gorgona Island, Colombia. *Contributions to Mineralogy and Petrology*, *86*, 94-105. doi: 10.1007/BF00373714

Bame, S. J., Asbridge, J. R., Feldman, W. C., Montgomery, M. D., & Kearney, P. D. (1975). Solar wind heavy ion abundances. *Solar Physics*, *43*, 463-473. doi: 10.1007/BF00152368

Bandfield, J. L., Poston, M. J., Klima, R. L., & Edwards, C. S. (2018). Widespread distribution of OH/H2O on the lunar surface inferred from spectral data. *Nature Geoscience*, *11*(3), 173-177. doi:10.1038/s41561-018-0065-0

Barraud, O., Besse, S., & Doressoundiram, A. (2023). Low sulfide concentration in Mercury's smooth plains inhibits hollows. *Science Advances*, *9*(12), eadd6452. doi: 10.1126/sciadv.add6452

Barraud, O., Doressoundiram, A., Besse, S., & Sunshine, J. M. (2020). Near-ultraviolet to near-infrared spectral properties of hollows on Mercury: Implications for origin and formation process. *Journal of Geophysical Research: Planets*, *125*(12), e2020JE006497. doi:10.1029/2020JE006497

Benkhoff, J., Murakami, G., Baumjohann, W., Besse, S., Bunce, E., Casale, M., ... & Zender, J. (2021). BepiColombo-mission overview and science goals. *Space science reviews*, *217*(8), 90. doi: 10.1007/s11214-021-00861-4

Bentley, M. S. (2005). *Space weathering on Mercury: Laboratory studies and modelling*. Open University (United Kingdom).

Blewett, D. T., Robinson, M. S., Denevi, B. W., Gillis-Davis, J. J., Head, J. W., Solomon, S. C., ... & McClintock, W. E. (2009). Multispectral images of Mercury from the first MESSENGER flyby: Analysis of global and regional color trends. *Earth and Planetary Science Letters*, *285*(3-4), 272-282. doi: 10.1016/j.epsl.2009.02.021

Blewett, D. T., Hawke, B. R., & Lucey, P. G. (2002). Lunar pure anorthosite as a spectral analog for Mercury. *Meteoritics & Planetary Science*, *37*(9), 1245-1254. doi: 10.1111/j.1945-5100.2002.tb00893.x

Bott, N., Brunetto, R., Doressoundiram, A., Carli, C., Capaccioni, F., Langevin, Y., ... & Sandt, C. (2023a). Effects of Temperature on Visible and Infrared Spectra of Mercury Minerals Analogues. *Minerals*, *13*(2), 250. doi: 10.3390/min13020250

Bott, N., Thompson, M. S., Vander Kaaden, K. E., Loeffler, M. J., & McCubbin, F. M. (2023b, March). Simulating Micrometeoroid Bombardment on Mercury: Identifying New Space Weathering Features in the Laboratory. In The 54th Lunar and Planetary Science Conference (LPSC 2023).

Boynton, W. V., Sprague, A. L., Solomon, S. C., Starr, R. D., Evans, L. G., Feldman, W. C., ... & Rhodes, E. A. (2007). MESSENGER and the chemistry of Mercury's surface. *Space science reviews*, *131*, 85-104. doi: 10.1007/s11214-007-9258-3

Brucato, J. R., Strazzulla, G., Baratta, G., & Colangeli, L. (2004). Forsterite amorphisation by ion irradiation: Monitoring by infrared spectroscopy. *Astronomy & Astrophysics*, *413*(2), 395-401. doi : 10.1051/0004-6361:20031574

Brucato, J. R., Palumbo, M. E., & Strazzulla, G. (1997). Carbonic acid by ion implantation in water/carbon dioxide ice mixtures. *Icarus*, *125*(1), 135-144. doi: 10.1006/icar.1996.5561

Brunetto, R., Lantz, C., Nakamura, T., Baklouti, D., Le Pivert-Jolivet, T., Kobayashi, S., & Borondics, F. (2020). Characterizing irradiated surfaces using IR spectroscopy. *Icarus*, *345*, 113722. doi: 10.1016/j.icarus.2020.113722

Brunetto, R., Lantz, C., Ledu, D., Baklouti, D., Barucci, M. A., Beck, P., ... & Dartois, E. (2014). Ion irradiation of Allende meteorite probed by visible, IR, and Raman spectroscopies. *Icarus*, *237*, 278-292. doi: 10.1016/j.icarus.2014.04.047

Brunetto, R., Vernazza, P., Marchi, S., Birlan, M., Fulchignoni, M., Orofino, V., & Strazzulla, G. (2006). Modeling asteroid surfaces from observations and irradiation experiments: The case of 832 Karin. *Icarus*, *184*(2), 327-337. doi: 10.1016/j.icarus.2006.05.019

Brunetto, R., & Strazzulla, G. (2005). Elastic collisions in ion irradiation experiments: A mechanism for space weathering of silicates. *Icarus*, *179*(1), 265-273. doi: 10.1016/j.icarus.2005.07.001

Bruschini, E., Carli, C., Buellet, A. C., Vincendon, M., Capaccioni, F., Ferrari, M., ... & Montanini, A. (2022). VNIR reflectance spectra of silicate-graphite mixtures: The effect of graphite content and particle size. *Icarus*, *378*, 114950. doi: 10.1016/j.icarus.2022.114950

Burns, R. G. (1993). *Mineralogical applications of crystal field theory* (No. 5). Cambridge university press.

Byrne, P. K., Ostrach, L. R., Fassett, C. I., Chapman, C. R., Denevi, B. W., Evans, A. J., ... & Solomon, S. C. (2016). Widespread effusive volcanism on Mercury likely ended by about 3.5 Ga. *Geophysical Research Letters*, *43*(14), 7408-7416. doi: 10.1002/2016GL069412.

Caminiti, E., Doressoundiram, A., Besse, S., & Wright, J. (2023). A spectral study of the Caloris basin on Mercury and the origin of associated volcanic smooth plains. *Journal of Geophysical Research: Planets*, e2022JE007685. doi: 10.1029/2022JE007685

Carrez, P., Demyk, K., Cordier, P., Gengembre, L., Grimblot, J., d'HENDECOURT, L., ... & Leroux, H. (2002). Low-energy helium ion irradiation-induced amorphization and chemical changes in olivine: Insights for silicate dust evolution in the interstellar medium. *Meteoritics & Planetary Science*, *37*(11), 1599-1614. doi: 10.1111/j.1945-5100.2002.tb00814.x

Carli, C., Serrano, L. M., Maturilli, A., Massironi, M., Capaccioni, F., & Helbert, J. (2013). VNIR and TIR Spectra of Terrestrial Komatiites Possibly Analogues of some Hermean Terrain Compositions. Poster.

Charlier, B., Grove, T. L., & Zuber, M. T. (2013). Phase equilibria of ultramafic compositions on Mercury and the origin of the compositional dichotomy. *Earth and Planetary Science Letters*, *363*, 50–60. doi: 10.1016/j.epsl.2012.12.021

Chauvin, N., Dayras, F., Le Du, D., & Meunier, R. (2004). SIDONIE: an electromagnetic isotope separator for preparation of high purity thin targets. *Nuclear Instruments and Methods in Physics Research Section A: Accelerators, Spectrometers, Detectors and Associated Equipment*, *521*(1), 149-155. doi: 10.1016/j.nima.2003.11.417

Chrbolková, K., Brunetto, R., Ďurech, J., Kohout, T., Mizohata, K., Malý, P., ... & Maturilli, A. (2021). Comparison of space weathering spectral changes induced by solar wind and micrometeoroid impacts using ion-and femtosecond-laser-irradiated olivine and pyroxene. *Astronomy & Astrophysics*, *654*, A143. doi: 10.1051/0004-6361/202140372

1116 Cremonese, G., Capaccioni, F., Capria, M. T., Doressoundiram, A., Palumbo, P., Vincendon, M., ... & Turrini, D. (2020).
1117 SIMBIO-SYS: scientific cameras and spectrometer for the BepiColombo mission. *Space science reviews*, *216*, 1-78. doi:
1118 10.1007/s11214-020-00704-8

1119 Demyk, K., Carrez, P., Leroux, H., Cordier, P., Jones, A. P., Borg, J., ... & d'Hendecourt, L. (2001). Structural and chemical
1120 alteration of crystalline olivine under low energy He+ irradiation. *Astronomy & Astrophysics*, *368*(3), L38-L41. doi:
1121 10.1051/0004-6361:20010208

1122 Denevi, B. W., Ernst, C. M., Meyer, H. M., Robinson, M. S., Murchie, S. L., Whitten, J. L., ... & Peplowski, P. N. (2013). The
1123 distribution and origin of smooth plains on Mercury. *Journal of Geophysical Research: Planets*, *118*(5), 891-907. doi:
1124 10.1002/jgre.20075

1125 Denevi, B. W., Robinson, M. S., Solomon, S. C., Murchie, S. L., Blewett, D. T., Domingue, D. L., et al. (2009). The evolution of
1126 Mercury's crust: A global perspective from MESSENGER. *Science*, *324*(5927), 613–618. doi: 10.1126/science.1172226

1127 Deutsch, A. N., Neumann, G. A., Kreslavsky, M. A., Pokorný, P., Camacho, J. M. M., Trang, D., ... & Filacchione, G. (2024).
1128 Temperature-related Variations of 1064 nm Surface Reflectance on Mercury: Implications for Space Weathering. *The*
1129 *Planetary Science Journal*, *5*(1), 8. doi: 10.3847/PSJ/ad0e6d

1130 D'Incecco, P., Helbert, J., D'Amore, M., Maturilli, A., Head, J. W., Klima, R. L., ... & Ferrari, S. (2015). Shallow crustal
1131 composition of Mercury as revealed by spectral properties and geological units of two impact craters. *Planetary and Space*
1132 *Science*, *119*, 250-263. doi: 10.1016/j.pss.2015.10.007

1133 Dionnet, Z., Aléon-Toppani, A., Brunetto, R., Rubino, S., Suttle, M. D., Lantz, C., ... & Scheel, M. (2022). Multiscale correlated
1134 analysis of the Aguas Zarcas CM chondrite. *Meteoritics & Planetary Science*, *57*(5), 965-988. doi: 10.1111/maps.13807

1135 Dukes, C. A., Fulvio, D., & Baragiola, R. A. (2015, November). Ion-irradiation induced changes in the surface composition of
1136 carbonaceous meteorites. In *Space Weathering of Airless Bodies: An Integration of Remote Sensing Data, Laboratory*
1137 *Experiments and Sample Analysis Workshop* (Vol. 1878, p. 2063).

1138 Dumas, P., Polack, F., Lagarde, B., Chubar, O., Giorgetta, J. L., & Lefrançois, S. (2006). Synchrotron infrared microscopy at
1139 the French Synchrotron Facility SOLEIL. *Infrared Physics & Technology*, *49*(1-2), 152-160. doi:
1140 10.1016/j.infrared.2006.01.030
1141
1142 Dunne, J. A., & Burgess, E. (1978). *The voyage of Mariner 10: mission to Venus and Mercury* (Vol. 424). Scientific and
1143 Technical Information Division, National Aeronautics and Space Administration.
1144
1145 Domingue, D. L., Chapman, C. R., Killen, R. M., Zurbuchen, T. H., Gilbert, J. A., Sarantos, M., ... & McClintock, W. E. (2014).
1146 Mercury's weather-beaten surface: Understanding Mercury in the context of lunar and asteroidal space weathering studies.
1147 *Space Science Reviews*, *181*, 121-214. doi: 10.1007/s11214-014-0039-5

1148 Ernst, C. M., Murchie, S. L., Barnouin, O. S., Robinson, M. S., Denevi, B. W., Blewett, D. T., et al. (2010). Exposure of
1149 spectrally distinct mate- rial by impact craters on Mercury: Implications for global stratigraphy. *Icarus*, *209*(1), 210–223. doi:
1150 10.1016/j.icarus.2010.05.022

Evans, L. G., Peplowski, P. N., Rhodes, E. A., Lawrence, D. J., McCoy, T. J., Nittler, L. R., ... & Goldsten, J. O. (2012). Major-element abundances on the surface of Mercury: Results from the MESSENGER Gamma-Ray Spectrometer. *Journal of Geophysical Research: Planets*, *117*(E12). doi: 10.1029/2012JE004178

Fu, X., Zou, Y., Zheng, Y., & Ouyang, Z. (2012). Effects of space weathering on diagnostic spectral features: Results from He+ irradiation experiments. *Icarus*, *219*(2), 630-640. doi: 10.1016/j.icarus.2012.03.009

Goudge, T. A., Head, J. W., Kerber, L., Blewett, D. T., Denevi, B. W., Domingue, D. L., ... & Solomon, S. C. (2014). Global inventory and characterization of pyroclastic deposits on Mercury: New insights into pyroclastic activity from MESSENGER orbital data. *Journal of Geophysical Research: Planets*, *119*(3), 635-658. doi: 10.1002/2013JE004480

Hapke, B. (2001). Space weathering from Mercury to the asteroid belt. *Journal of Geophysical Research: Planets*, *106*(E5), 10039-10073. doi: 10.1029/2000JE001338

Head, J. W., Chapman, C. R., Strom, R. G., Fassett, C. I., Denevi, B. W., Blewett, D. T., et al. (2011). Flood volcanism in the northern high lati- tudes of Mercury revealed by MESSENGER. *Science*, *333*(6051), 1853–1856. doi: 10.1126/science.1211997

Helbert, J., Maturilli, A., & D'Amore, M. (2013). Visible and near-infrared reflectance spectra of thermally processed synthetic sulfides as a potential analog for the hollow forming materials on Mercury. *Earth and Planetary Science Letters*, *369*, 233-238. doi: 10.1016/j.epsl.2013.03.045

Hiesinger, H., Helbert, J., Alemanno, G., Bauch, K. E., D'Amore, M., Maturilli, A., ... & MERTIS Co-I Team. (2020). Studying the composition and mineralogy of the Hermean surface with the Mercury Radiometer and Thermal Infrared Spectrometer (MERTIS) for the BepiColombo mission: an update. *Space Science Reviews*, *216*, 1-37. doi: 10.1007/s11214-020-00732-4

Hijazi, H., Bannister, M. E., Meyer III, H. M., Rouleau, C. M., & Meyer, F. W. (2017). Kinetic and potential sputtering of an anorthite-like glassy thin film. Journal of Geophysical Research: Planets, 122(7), 1597-1609. doi: 10.1002/2017JE005300

Izenberg, N. R., Klima, R. L., Murchie, S. L., Blewett, D. T., Holsclaw, G. M., McClintock, W. E., ... & Dyar, M. D. (2014). The low-iron, reduced surface of Mercury as seen in spectral reflectance by MESSENGER. *Icarus*, *228*, 364-374. doi: 10.1016/j.icarus.2013.10.023

Jäger, C., Fabian, D., Schrempel, F., Dorschner, J., Henning, T., & Wesch, W. (2003). Structural processing of enstatite by ion bombardment. *Astronomy & Astrophysics*, *401*(1), 57-65. doi: 10.1051/0004-6361:20030002

Jäggi, N., Galli, A., Wurz, P., Biber, H., Szabo, P. S., Brötzner, J., ... & Mezger, K. (2021). Creation of Lunar and Hermean analogue mineral powder samples for solar wind irradiation experiments and mid-infrared spectra analysis. *Icarus*, *365*, 114492. doi: 10.1016/j.icarus.2021.114492

Johnson, R. E. 1990, in Energetic charged–Particle Interactions with Atmospheres and Surfaces, Physics and Chemistry in Space Planetology, Vol. 19, ed. L. J. Lanzerotti, M. Hill, & D. Stoffler Munster (Berlin: Springer), 232

Killen, R., Cremonese, G., Lammer, H., Orsini, S., Potter, A. E., Sprague, A. L., ... & Mura, A. (2007). Processes that promote and deplete the exosphere of Mercury. *Space Science Reviews*, *132*, 433-509. doi: 10.1007/s11214-007-9232-0

Klima, R. L., Izenberg, N. R., Murchie, S., Meyer, H. M., Stockstill-Cahill, K. R., Blewett, D. T., ... & Weider, S. Z. (2013, March). Constraining the ferrous iron content of silicate minerals in Mercury's crust. In *44th Annual Lunar and Planetary Science Conference* (No. 1719, p. 1602).

Langevin, Y. (1997). The regolith of Mercury: present knowledge and implications for the Mercury Orbiter mission. *Planetary and space science*, *45*(1), 31-37. doi: 10.1016/S0032-0633(96)00098-0

Lantz, C., Brunetto, R., Barucci, M. A., Fornasier, S., Baklouti, D., Bourçois, J., & Godard, M. (2017). Ion irradiation of carbonaceous chondrites: A new view of space weathering on primitive asteroids. *Icarus*, *285*, 43-57. doi: 10.1016/j.icarus.2016.12.019

Lantz, C., Brunetto, R., Barucci, M. A., Dartois, E., Duprat, J., Engrand, C., ... & Quirico, E. (2015). Ion irradiation of the Murchison meteorite: Visible to mid-infrared spectroscopic results. *Astronomy & Astrophysics*, *577*, A41. doi: 10.1051/0004-6361/201425398

Lavorenti, F., Jensen, E. A., Aizawa, S., Califano, F., D'Amore, M., Domingue, D., ... & Savin, D. W. (2023). Maps of solar wind plasma precipitation onto Mercury's surface: a geographical perspective. *arXiv preprint arXiv:2305.09498*. doi: 10.48550/arXiv.2305.09498

Le Bas, M. J. (2000). IUGS reclassification of the high-Mg and picritic volcanic rocks. *Journal of Petrology*, *41*(10), 1467-1470. doi: 10.1093/petrology/41.10.1467

Liu, Y., Guan, Y., Zhang, Y., Rossman, G. R., Eiler, J. M., & Taylor, L. A. (2012). Direct measurement of hydroxyl in the lunar regolith and the origin of lunar surface water. *Nature Geoscience*, *5*(11), 779-782. doi:10.1038/ngeo1601

Loeffler, M. J., Dukes, C. A., & Baragiola, R. A. (2009). Irradiation of olivine by 4 keV He+: Simulation of space weathering by the solar wind. *Journal of Geophysical Research: Planets*, *114*(E3). doi: 10.1029/2008JE003249

Lucey, P. G., & Riner, M. A. (2011). The optical effects of small iron particles that darken but do not redden: Evidence of intense space weathering on Mercury. *Icarus*, *212*(2), 451-462. doi: 10.1016/j.icarus.2011.01.022

Lucey, P. G., & Noble, S. K. (2008). Experimental test of a radiative transfer model of the optical effects of space weathering. *Icarus*, *197*(1), 348-353. doi:10.1016/j.icarus.2008.05.008

Marchi, S., Brunetto, R., Magrin, S., Lazzarin, M., & Gandolfi, D. (2005). Space weathering of near-Earth and main belt silicate-rich asteroids: observations and ion irradiation experiments. *Astronomy & Astrophysics*, *443*(3), 769-775. doi: 10.1051/0004-6361:20053525

Mari, N., Eggers, G. L., Filiberto, J., Carli, C., Pratesi, G., Alvaro, M., ... & Di Achille, G. (2023). Boninites as Mercury lava analogues: Geochemical and spectral measurements from pillow lavas on Cyprus island. *Planetary and Space Science*, 105764. https://doi.org/10.1016/j.pss.2023.105764

Mason, G. M., Leske, R. A., Desai, M. I., Cohen, C. M., Dwyer, J. R., Mazur, J. E., ... & Krimigis, S. M. (2008). Abundances and energy spectra of corotating interaction region heavy ions observed during solar cycle 23. *The Astrophysical Journal*, *678*(2), 1458. doi:10.1086/533524

Massetti, S., Orsini, S., Milillo, A., & Mura, A. (2007). Modelling Mercury's magnetosphere and plasma entry through the dayside magnetopause. *Planetary and Space Science*, *55*(11), 1557-1568. doi: 10.1016/j.pss.2006.12.008

Matsumoto, T., Tsuchiyama, A., Miyake, A., Noguchi, T., Nakamura, M., Uesugi, K., ... & Nakano, T. (2015). Surface and internal structures of a space-weathered rim of an Itokawa regolith particle. *Icarus*, *257*, 230-238. doi: 10.1016/j.icarus.2015.05.001

Maturilli, A., Helbert, J., John, J. M. S., Head, J. W., III., Vaughan, W. M., D'Amore, M., et al. (2014). Komatiites as Mercury surface analogues: Spectral measurements at PEL. *Earth and Planetary Science Letters*, *398*, 58–65. doi: 10.1016/j.epsl.2014.04.035

McClintock, W. E., Izenberg, N. R., Holsclaw, G. M., Blewett, D. T., Domingue, D. L., Head III, J. W., ... & Vilas, F. (2008). Spectroscopic observations of Mercury's surface reflectance during MESSENGER's first Mercury flyby. *Science*, *321*(5885), 62-65. doi: 10.1126/science.1159933

McKay, D. S., Heiken, G., Basu, A., Blanford, G., Simon, S., Reedy, R., ... & Papike, J. (1991). The lunar regolith. *Lunar sourcebook*, *567*, 285-356.

McNutt, R. L., Jr., Solomon, S. C., Gold, R. E., Leary, J. C., & MESSENGER Team. (2006). The MESSENGER mission to Mercury: Develop- ment history and early mission status. *Advances in Space Research*, *38*(4), 564–571. doi: 10.1016/j.asr.2005.05.044

Mewaldt, R. A., Cohen, C. M. S., Mason, G. M., Cummings, A. C., Desai, M. I., Leske, R. A., ... & Zurbuchen, T. H. (2007). On the differences in composition between solar energetic particles and solar wind. *Space science reviews*, *130*, 207-219. doi:10.1007/s11214-007-9187-1

Meyer-Vernet, N. (2007). *Basics of the solar wind*. Cambridge University Press.

Morlok, A., Renggli, C., Charlier, B., Namur, O., Klemme, S., Reitze, M. P., ... & Helbert, J. (2023). A mid-infrared study of synthetic glass and crystal mixtures analog to the geochemical terranes on mercury. *Icarus*, *396*, 115498. doi: 10.1016/j.icarus.2023.115498

Morlok, A., Renggli, C., Charlier, B., Reitze, M. P., Klemme, S., Namur, O., ... & Helbert, J. (2021). Mid-infrared reflectance spectroscopy of synthetic glass analogs for Mercury surface studies. *Icarus*, *361*, 114363. doi: 10.1016/j.icarus.2021.114363

Morlok, A., Klemme, S., Weber, I., Stojic, A., Sohn, M., Hiesinger, H., & Helbert, J. (2019). Mid-infrared spectroscopy of planetary analogs: A database for planetary remote sensing. *Icarus*, *324*, 86-103. doi: 10.1016/j.icarus.2019.02.010

Morlok, A., Klemme, S., Weber, I., Stojic, A., Sohn, M., & Hiesinger, H. (2017). IR spectroscopy of synthetic glasses with Mercury surface composition: Analogs for remote sensing. *Icarus*, *296*, 123-138. doi: 10.1016/j.icarus.2017.05.024

Murchie, S. L., Klima, R. L., Denevi, B. W., Ernst, C. M., Keller, M. R., Domingue, D. L., et al. (2015). Orbital multispectral mapping of Mercury with the MESSENGER Mercury Dual Imaging System: Evidence for the origins of plains units and low-reflectance material. *Icarus*, *254*, 287–305. doi: 10.1016/j.icarus.2015.03.027

Namur, O., & Charlier, B. (2017). Silicate mineralogy at the surface of Mercury. *Nature Geoscience*, *10*(1), 9–13. doi: 10.1038/ ngeo2860

Nash, D. B., & Salisbury, J. W. (1991). Infrared reflectance spectra (2.2–15 μm) of plagioclase feldspars. *Geophysical Research Letters*, *18*(6), 1151-1154. doi: 10.1029/91GL01008

Nittler, L. R., Frank, E. A., Weider, S. Z., Crapster-Pregont, E., Vorburger, A., Starr, R. D., & Solomon, S. C. (2020). Global major-element maps of Mercury from four years of MESSENGER X-Ray Spectrometer observations. *Icarus*, *345*, 113716. doi: 10.1016/j.icarus.2020.113716

Nittler, L. R., & Weider, S. Z. (2019). The surface composition of Mercury. *Elements: An International Magazine of Mineralogy, Geochemistry, and Petrology*, *15*(1), 33-38. doi: 10.2138/gselements.15.1.33

Nittler, L. R., Starr, R. D., Weider, S. Z., McCoy, T. J., Boynton, W. V., Ebel, D. S., ... & Sprague, A. L. (2011). The major-element composition of Mercury's surface from MESSENGER X-ray spectrometry. *Science*, *333*(6051), 1847-1850. doi: 10.1126/science.1211567

Nittler, L. R., McCoy, T. J., Clark, P. E., Murphy, M. E., Trombka, J. I., & Jarosewich, E. (2004). Bulk element compositions of meteorites: A guide for interpreting remote-sensing geochemical measurements of planets and asteroids. *Antarctic Meteorite Research*

Nittler, L. R., Starr, R. D., Lim, L., Mccoy, T. J., Burbine, T. H., Reedy, R. C., ... & Killen, R. (2001). X-ray fluorescence measurements of the surface elemental composition of asteroid 433 Eros. *Meteoritics & Planetary Science*, *36*(12), 1673-1695. doi: 10.1111/j.1945-5100.2001.tb01856.x

Noble, S. K., Pieters, C. M., & Keller, L. P. (2007). An experimental approach to understanding the optical effects of space weathering. *Icarus*, *192*(2), 629-642. doi: 10.1016/j.icarus.2007.07.021

Noble, S. K., & Pieters, C. M. (2003). Space weathering on Mercury: Implications for remote sensing. *Solar System Research*, *37*, 31-35. doi: 10.1023/A:1022395605024

Noble, S. K., Pieters, C. M., Taylor, L. A., Morris, R. V., Allen, C. C., McKAY, D. S., & Keller, L. P. (2001). The optical properties of the finest fraction of lunar soil: Implications for space weathering. *Meteoritics & Planetary Science*, *36*(1), 31-42. doi: 10.1111/j.1945-5100.2001.tb01808.x

Ogilvie, K. W., Scudder, J. D., Hartle, R. E., Siscoe, G. L., Bridge, H. S., Lazarus, A. J., ... & Yeates, C. M. (1974). Observations at Mercury encounter by the plasma science experiment on Mariner 10. *Science*, *185*(4146), 145-151. doi: 10.1126/science.185.4146.145

Pearce, J. A., & Reagan, M. K. (2019). Identification, classification, and interpretation of boninites from Anthropocene to Eoarchean using Si-Mg-Ti systematics. *Geosphere*, *15*(4), 1008-1037. doi: 10.1130/GES01661.1

Penttilä, A., Väisänen, T., Markkanen, J., Martikainen, J., Kohout, T., Videen, G., & Muinonen, K. (2020). Rigorous light-scattering simulations of nanophase iron space-weathering effects on reflectance spectra of olivine grains. *Icarus*, *345*, 113727. doi: 10.1016/j.icarus.2020.113727

Peplowski, P. N., & Stockstill-Cahill, K. (2019). Analytical identification and characterization of the major geochemical terranes of Mercury's northern hemisphere. *Journal of Geophysical Research: Planets*, *124*(9), 2414-2429. doi: 10.1029/2019JE005997

Peplowski, P. N., Lawrence, D. J., Feldman, W. C., Goldsten, J. O., Bazell, D., Evans, L. G., et al. (2015). Geochemical terranes of Mercury's northern hemisphere as revealed by MESSENGER neutron measurements. *Icarus*, *253*, 346–363. doi: 10.1016/j.icarus.2015.02.002

Pieters, C. M., & Noble, S. K. (2016). Space weathering on airless bodies. *Journal of Geophysical Research: Planets*, *121*(10), 1865-1884. doi: 10.1002/2016JE005128

Pisello, A., Bisolfati, M., Poggiali, G., Tolomei, P., Braschi, E., Brucato, J. R., & Perugini, D. (2023). Mid-Infrared (MIR) Spectroscopy of Silicate Glasses as Analogs for Mercury's Surface: The Influence of Grain Size. *Minerals*, *13*(2), 170. doi: 10.3390/min13020170

Raines, J. M., Dewey, R. M., Staudacher, N. M., Tracy, P. J., Bert, C. M., Sarantos, M., ... & Slavin, J. A. (2022). Proton precipitation in Mercury's northern magnetospheric cusp. *Journal of Geophysical Research: Space Physics*, *127*(11), e2022JA030397. doi: 10.1029/2022JA030397

Reitze, M. P., Weber, I., Morlok, A., Hiesinger, H., Bauch, K. E., Stojic, A. N., & Helbert, J. (2021). Mid-infrared spectroscopy of crystalline plagioclase feldspar samples with various Al, Si order and implications for remote sensing of Mercury and other terrestrial Solar System objects. *Earth and Planetary Science Letters*, *554*, 116697. doi: 10.1016/j.epsl.2020.116697

Riner, M. A., & Lucey, P. G. (2012). Spectral effects of space weathering on Mercury: The role of composition and environment. *Geophysical research letters*, *39*(12). doi: 10.1029/2012GL052065

Robinson, M. S., Murchie, S. L., Blewett, D. T., Domingue, D. L., Hawkins, S. E., III, Head, J. W., et al. (2008). Reflectance and color variations on Mercury: Regolith processes and compositional heterogeneity. *Science*, *321*(5885), 66–69. doi: 10.1126/science.1160080

Rubino, S., Leroux, H., Lantz, C., Aléon-Toppani, A., Baklouti, D., Djouadi, Z., ... & Brunetto, R. (2024). Space-weathering induced changes in hydrated silicates: A multi-scale study combining visible/infrared spectroscopy and electron microscopy. *Icarus*, 116070. doi: 10.1016/j.icarus.2024.116070

Rubino, S., Lantz, C., Baklouti, D., Leroux, H., Borondics, F., & Brunetto, R. (2020). Space weathering affects the remote near-IR identification of phyllosilicates. *The Planetary Science Journal*, *1*(3), 61. doi : 10.3847/PSJ/abb94c

Salisbury, J. W., D'Aria, D. M., & Jarosewich, E. (1991). Midinfrared (2.5–13.5 µm) reflectance spectra of powdered stony meteorites. *Icarus*, *92*(2), 280-297. doi: 10.1016/0019-1035(91)90052-U

Sarantos, M., Killen, R. M., & Kim, D. (2007). Predicting the long-term solar wind ion-sputtering source at Mercury. *Planetary and Space Science*, *55*(11), 1584-1595. doi: 10.1016/j.pss.2006.10.011

Sasaki, S., & Kurahashi, E. (2004). Space weathering on Mercury. *Advances in Space Research*, *33*(12), 2152-2155. doi: 10.1016/S0273-1177(03)00442-3

Serrano, L., Ferrari, L., Martínez, M. L., Petrone, C. M., & Jaramillo, C. (2011). An integrative geologic, geochronologic and geochemical study of Gorgona Island, Colombia: Implications for the formation of the Caribbean Large Igneous Province. *Earth and Planetary Science Letters*, *309*(3-4), 324-336. doi: 10.1016/j.epsl.2011.07.011

Serrano Durán, Lina María. (2009). "Origen de la Isla Gorgona (Colombia) y su relación con el Plateau del Caribe". (Tesis de Maestría). Universidad Nacional Autónoma de México, México. Recuperado de https://repositorio.unam.mx/contenidos/89624

Solomon, S. C., McNutt, R. L., Gold, R. E., & Domingue, D. L. (2007). MESSENGER mission overview. *Space Science Reviews*, *131*(1–4), 3–39. doi: 10.1007/s11214-007-9247-6

Sprague, A. L., Emery, J. P., Donaldson, K. L., Russell, R. W., Lynch, D. K., & Mazuk, A. L. (2002). Mercury: Mid-infrared (3–13.5 µm) observations show heterogeneous composition, presence of intermediate and basic soil types, and pyroxene. *Meteoritics & Planetary Science*, *37*(9), 1255-1268. doi: 10.1111/j.1945-5100.2002.tb00894.x

Stockstill-Cahill, K. R., McCoy, T. J., Nittler, L. R., Weider, S. Z., & Hauck, S. A. (2012). Magnesium-rich crustal compositions on Mercury: Implications for magmatism from petrologic modeling. *Journal of Geophysical Research*, *117*(E12), E00L15. doi: 10.1029/2012JE004140

Strazzulla, G., Dotto, E., Binzel, R., Brunetto, R., Barucci, M. A., Blanco, A., & Orofino, V. (2005). Spectral alteration of the Meteorite Epinal (H5) induced by heavy ion irradiation: a simulation of space weathering effects on near-Earth asteroids. *Icarus*, *174*(1), 31-35. doi: 10.1016/j.icarus.2004.09.013

Sultana, R., Poch, O., Beck, P., Schmitt, B., & Quirico, E. (2021). Visible and near-infrared reflectance of hyperfine and hyperporous particulate surfaces. *Icarus*, *357*, 114141. doi: 10.1016/j.icarus.2020.114141

Szabo, P. S., Biber, H., Jäggi, N., Brenner, M., Weichselbaum, D., Niggas, A., ... & Aumayr, F. (2020). Dynamic potential sputtering of lunar analog material by solar wind ions. *The Astrophysical Journal*, *891*(1), 100. doi:10.3847/1538-4357/ab7008

Thompson, M. S., Vander Kaaden, K. E., Loeffler, M. J., & Mccubbin, F. M. (2021, March). Understanding the space weathering of Mercury through laboratory experiments. In Lunar and Planetary Science Conference.

Trang, D., Lucey, P. G., & Izenberg, N. R. (2017). Radiative transfer modeling of MESSENGER VIRS spectra: Detection and mapping of submicroscopic iron and carbon. *Icarus*, *293*, 206-217. doi: 10.1016/j.icarus.2017.04.026

Vander Kaaden, K. E., McCubbin, F. M., Nittler, L. R., Peplowski, P. N., Weider, S. Z., Frank, E. A., & McCoy, T. J. (2017). Geochemistry, mineralogy, and petrology of boninitic and komatiitic rocks on the mercurian surface: Insights into the mercurian mantle. *Icarus*, *285*, 155-168. doi: 10.1016/j.icarus.2016.11.041

Vander Kaaden, K. E., & McCubbin, F. M. (2016). The origin of boninites on Mercury: An experimental study of the northern volcanic plains lavas. *Geochimica et Cosmochimica Acta*, *173*, 246–263. doi: 10.1016/j.gca.2015.10.016

Vernazza, P., Fulvio, D., Brunetto, R., Emery, J. P., Dukes, C. A., Cipriani, F., ... & Baragiola, R. A. (2013). Paucity of Tagish Lake-like parent bodies in the Asteroid Belt and among Jupiter Trojans. *Icarus*, *225*(1), 517-525. doi: 10.1016/j.icarus.2013.04.019

Vilas, F. (1985). Mercury: Absence of crystalline Fe2+ in the regolith. *Icarus*, *64*(1), 133-138. doi: 10.1016/0019-1035(85)90044-2

Wang, Y., Xiao, Z., Chang, Y., & Cui, J. (2020). Lost volatiles during the formation of hollows on Mercury. *Journal of Geophysical Research: Planets*, *125*(9), e2020JE006559. doi: 10.1029/2020JE006559

Warell, J., Sprague, A., Kozlowski, R., Rothery, D. A., Lewis, N., Helbert, J., & Cloutis, E. (2010). Constraints on Mercury's surface composition from MESSENGER and ground-based spectroscopy. *Icarus*, *209*(1), 138-163. doi: 10.1016/j.icarus.2010.04.008

Warell, J., Sprague, A. L., Emery, J. P., Kozlowski, R. W. H., & Long, A. (2006). The 0.7–5.3 µm IR spectra of Mercury and the Moon: Evidence for high-Ca clinopyroxene on Mercury. *Icarus*, *180*(2), 281-291. doi: 10.1016/j.icarus.2005.09.007

Warell, J. (2002). Properties of the Hermean regolith: II. Disk-resolved multicolor photometry and color variations of the "unknown" hemisphere. *Icarus*, *156*(2), 303-317. doi: 10.1006/icar.2002.6814

Weber, I., Morlok, A., Heeger, C., Adolphs, T., Reitze, M., Hiesinger, H., ... & Helbert, J. (2019). Simulating space weathering on Mercury: excimer laser experiments on mineral mixtures. Lunar Planet. Sci. 50, 2326 (2019)

Weider, S. Z., Nittler, L. R., Starr, R. D., Crapster-Pregont, E. J., Peplowski, P. N., Denevi, B. W., et al. (2015). Evidence for geochemical terranes on Mercury: Global mapping of major elements with MESSENGER's X-ray spectrometer. *Earth and Planetary Science Letters*, *416*, 109–120. doi: 10.1016/j.epsl.2015.01.023

1416 Weider, S. Z., Nittler, L. R., Starr, R. D., McCoy, T. J., & Solomon, S. C. (2014). Variations in the abundance of iron on
1417 Mercury's surface from MESSENGER X-Ray Spectrometer observations. *Icarus*, *235*, 170-186. doi:
1418 10.1016/j.icarus.2014.03.002

1419 Weider, S. Z., Nittler, L. R., Starr, R. D., McCoy, T. J., Stockstill-Cahill, K. R., Byrne, P. K., ... & Solomon, S. C. (2012). Chemical
1420 heterogeneity on Mercury's surface revealed by the MESSENGER X-Ray Spectrometer. *Journal of Geophysical Research:*
1421 *Planets*, *117*(E12). doi: 10.1029/2012JE004153

1422 Wilson, J. T., Lawrence, D. J., Peplowski, P. N., & Feldman, W. C. (2019). MESSENGER gamma ray spectrometer and
1423 epithermal neutron hydrogen data reveal compositional differences between Mercury's hot and cold poles. *Journal of*
1424 *Geophysical Research: Planets*, *124*(3), 721-733. doi: 10.1029/2018JE005871

1425 Wright, J., Byrne, P. K., & Rothery, D. A. (2021). Planet Mercury: Volcanism in a theatre of global contraction, with examples
1426 from the Hokusai quadrangle. *Journal of Volcanology and Geothermal Research*, *417*, 107300. doi:
1427 10.1016/j.jvolgeores.2021.107300

1428 Wurz, P., Whitby, J. A., Rohner, U., Martín-Fernández, J. A., Lammer, H., & Kolb, C. (2010). Self-consistent modelling of
1429 Mercury's exosphere by sputtering, micro-meteorite impact and photon-stimulated desorption. *Planetary and Space*
1430 *Science*, *58*(12), 1599-1616. doi: 10.1016/j.pss.2010.08.003